ORIGINAL PAPER

A Hybrid Approach to Rock Pre-conditioning Using Non-explosive Demolition Agents and Hydraulic Stimulation

V. R. S. De Silva[1,2,3] · **H. Konietzky**[2] · **H. Mearten**[3] · **P. G. Ranjith**[4] · **W. G. P. Kumari**[5]

Abstract

This study presents a novel approach to rock pre-conditioning to promote the sustainability of low-grade ore mining applications such as in-situ recovery and cave mining. The proposed method involves a two-stage hybrid approach, utilizing soundless cracking demolition agents (SCDAs) to initiate radial fractures in a predrilled host rock, followed by hydraulic stimulation to extend the fractures. SCDA injection in the first stage creates multiple radial fractures around the injection well. However, the extent of fractures is limited to the near vicinity of the injection well. To overcome this limitation, the second stage involves the application of hydraulic stimulation to extend the initiated fractures, which produces a greater fracture density compared to pure hydraulic stimulation. The concept was assessed using a fully coupled hydro-mechanical discrete element model that simulated the hybrid fracturing method on crystalline rock at the grain scale. The results indicate that the proposed method can create a high density of fractures around the injection well. Additionally, we identify and evaluate the key factors affecting the performance of the proposed method, including rock mass heterogeneity, stress anisotropy, and pre-existing defects, providing valuable insights for further experimental design and execution. Overall, the study offers promising results for a potential solution to enhance the efficiency of low-grade ore mining through the hybrid rock pre-conditioning method.

Highlights

- A novel hybrid two-stage pre-conditioning technique for low-grade ore recovery using soundless cracking demolition agents and hydraulic stimulation.
- A fully coupled hydro-mechanical model in the grain scale using the discrete element method to simulate the hybrid pre-conditioning technique.
- The hybrid method produces multiple radial fractures around an injection well, regardless of in-situ stress anisotropy.
- The hybrid method reduces the risk of uncontrolled fracture propagation by lowering the breakdown pressure of hydraulic stimulation.

✉ V. R. S. De Silva
    radhika.desilva@erdw.ethz.ch

1   Department of Earth Sciences, ETH Zürich, Sonneggstrasse 5, 8092 Zurich, Switzerland

2   Institut für Geotechnik, Technische Universität Bergakademie Freiberg, Akademiestraße 6, 09599 Freiberg, Germany

3   Umwelt- und Ingenieurtechnik GmbH, Dresden, Germany

4   Deep Earth Energy Laboratory, Department of Civil Engineering, Monash University, Building 60, Victoria 3800, Australia

5   School of Civil, Mining, and Environmental Engineering, Faculty of Engineering and Information Sciences, University of Wollongong, Wollongong, Australia

1 Introduction

The global decline in ore grades (Haque 2022) has led to an increased interest in mining technologies for processing low-grade ore. Cave mining also referred to as block caving (Morrison 2022) and In-Situ Recovery (ISR) (Wang et al. 2022b) have been identified as cost-effective methods to exploit low-grade ore. The widescale industry adaptation of these technologies relies on the general applicability of the techniques in different ore bodies. Fluid-based pre-conditioning or hydraulic fracturing is being explored as a potential technique to increase the range of applications of low-grade mining methods.

1.1 Hydraulic Stimulation in Cave Mining

The use of hydraulic stimulation (HS) for rock mass pre-conditioning in cave mining applications has seen an increase in recent years following its success in the oil and gas industry (He et al. 2016). Hydraulic stress stimulation introduces additional joint sets in a target rock formation which improves the fragmentation of a target ore body. Although cave mining is typically adopted in formations that are sufficiently weak to unravel under gravity loading, hydraulic stimulation methods have the potential to expand the application horizon of cave mining by artificially weakening (pre-conditioning) a target rock formation.

Several hydraulic stimulation projects were performed over the years to improve block caving which includes Northparkes mines copper/gold deposits (Jeffrey et al. 2009) and Newcrest Cadia East Mine (Amorer et al. 2022; Kaiser et al. 2013) in Australia, Tashan coal mine (Huang et al. 2018) and Anshan iron mine (Li et al. 2020) in China, Berezovskaya mine (Lekontsev and Sazhin 2008) in Russia, Salvador copper mine (Chacon et al. 2004) and El Teniente Mine in Morales et al. (2007) in Chile. These case studies indicate that hydraulic stimulation is innately dependent on the in-situ stress condition. The resultant fracture due to the hydraulic loading of an injection well propagates in the major principal stress direction (Chen et al. 2018). In addition, the fracturing fluid viscosity and the injection rate are two other parameters governing the fracture pattern in HS pre-conditioning applications (Bunger and Lecampion 2017). In the presence of natural fractures, HS was found to increase the number of fractures of an existing fracture network, whereas, for cave mining, it is favorable to induce additional fractures that intersect natural fractures leading to a blocky ore body.

1.2 Hydraulic Stimulation in ISR Applications

Hydraulic stimulation has been considered a potential pre-conditioning method to improve host-rock permeability in ISR. ISR is a non-invasive mining method that utilizes the intrinsic permeability of an ore deposit to inject a lixiviant that dissolves and extracts target minerals with minimal ground disturbance. In ISR, a series of injection and extraction wells are drilled into the target formation for the lixiviant circulation. HS was also adopted for artificial permeability enhancement in some ISR mining applications. Field trials of ISR projects included Mount Isa and Gunpowder copper mines in Australia (Seredkin et al. 2016), Kimbley pit (Ahlness and Pojar 1983), Van Dyke Copper mine (Huff et al. 1988) in the USA, and Chuqui Sur Deposit (Pallauta 1985) in Chile. However, these trials lack an in-depth understanding of the mechanics associated with HS pre-conditioning for mining applications.

1.3 The Gap

According to Bunger and Lecampion (2017), the four critical issues that require addressing for conventional HS applications in oil and gas reservoirs are: (1) controlling fracture height growth, (2) reducing fracture tortuosity near-wellbore, (3) predicting/modelling localized growth geometry, and (4) stimulation of multiple fractures simultaneously. From, a mining perspective, HS pre-conditioning is much smaller in scale compared to the oil and gas industry. For instance, the injection volume, rate and fracture extent for mining applications vary in the range of 8–20 m^3, 5–10 l/s and 1–2.5 m respectively while in the oil and gas industry, a typical well requires about 1000 m^3 fluid at a rate of 250 l/s, and the fracture extent is in the order of 100 s of meters (Adams and Rowe 2013; Bunger et al. 2012). At smaller-scale mining applications, issues (3) and (4) take precedence. He et al. (2017) and Zeeb and Konietzky (2015) proposed several options to overcome some aspects such as stress shadowing and producing prescribed fractures in a formation using directional hydraulic stimulation and hydraulic stimulation with perforations. However, technologies for pre-conditioning methods for mining applications require further research.

In this paper, we present a conceptual hybrid pre-conditioning method that addresses the issue of inducing multiple fractures. A two-stage fracturing process is proposed that utilizes a soundless cracking demolition agent (SCDA) (De Silva et al. 2018a) to initiate fractures in an injection
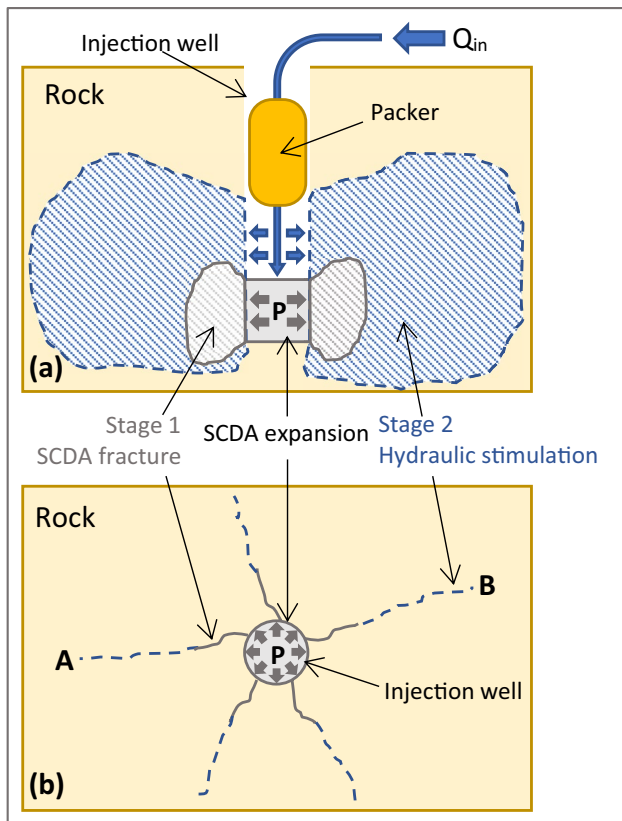
Fig. 1 The hybrid SCDA-HS injection method. Stage 1 SCDA injection and stage 2 hydraulic stimulation **a** section along A–B, and **b** plan view

well, followed by HS to simultaneously extend the initiated fractures. First, a grain scale numerical model using the 3 Dimensional Discrete Element Modelling software 3DEC 7.0 (Itasca 2022) is presented considering the material heterogeneity of a target rock mass. This is used to simulate SCDA-charged fracturing. Next, a fully coupled hydromechanical model simulating hydraulic fracturing at the grain scale is presented. This simulates hydraulic fracture extension. Finally, the model is used to assess the fracturing performance of the proposed hybrid fracturing method under varying in-situ stress conditions and micro-mechanical discontinuities. The proposed method shows promising results that can be used as a precursor to design and execute laboratory/field trials in unconventional low-grade ore mining methods such as cave mining, and permeability-enhanced in-situ recovery (ISR).

1.4 The Hybrid SCDA-HS Method

The proposed method consists of injecting SCDA slurry into a predrilled borehole to initiate fractures followed by HS to extend the initiated fractures (Fig. 1a). SCDA is a non-explosive demolition agent capable of generating expansive pressure inside a confined space. SCDAs have also been modified, specifically for subsurface applications below the water table which extends its usefulness to pre-conditioning for permeability-enhanced ISR (De Silva et al. 2018a). It mainly consists of calcium oxide (CaO), which forms an injectable slurry when mixed with water. During hydration, the SCDA slurry solidifies and expands volumetrically in an exothermic reaction producing $Ca(OH)_2$ (Eq. 1). The expansive pressure induced by SCDA in a pre-drilled injection well produces radial compressive stresses and tangential tensile stresses around the injection well (over 180 MPa according to experimental results of Natanzi et al. (2016)). Fractures are initiated around the surrounding rock when the tensile capacity of the rock is exceeded. After the first crack initiation, additional radial tensile cracks are formed due to the dissipation of strain energy by SCDA expansion (Fig. 1b). However, the extent of the fracture growth is primarily dependent on the in-situ stress conditions (De Silva et al. 2023) and is typically limited to the near vicinity of the injection well. Therefore, practical applications of SCDA charging require a secondary stage of fracture extension.

The hybrid method considers the extension of multiple radial fractures initiated by SCDA charging using HS. During the volumetric expansion process, the SCDA slurry transforms into a solid state. Following the first stage of fracturing, the solidified SCDA may be drilled out from the borehole. During the second stage of fracture extension, the SCDA-charged area may be isolated by a packer system and hydraulically restimulated to extend the initiated radial fractures. This process was numerically simulated in this study to assess its viability as a potential pre-conditioning technique.

$$CaO + H_2O \rightarrow Ca(OH)_2 \uparrow \Delta Hr = -\ 63.6 \ \ kJ/mol \qquad (1)$$

2 Methods

2.1 Numerical Simulation of the Hybrid SCDA-HS Method

Micro-mechanical properties affecting fracture initiation and propagation must be well understood for the intended applications of block caving and ISR. Therefore, a grain scale model was produced to understand the fracture mechanics in the rock mass that falls below the representative elementary volume, where the fracture initiation and evolution are heavily dependent on material heterogeneity and pre-existing defects (Fig. 2). The numerical model in 3DEC was developed in four steps. (1) An intact rock model was produced and calibrated at the grain scale using Voronoi tessellation
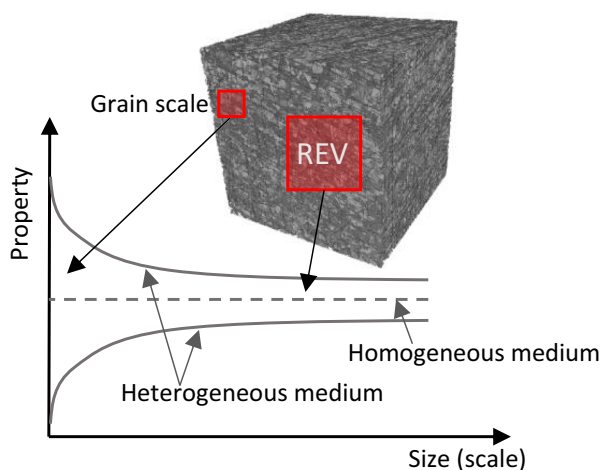
Fig. 2 The dependency of rock mass properties on the scale and the selection of the representative elementary volume (modified after Bear (1988) and Farahmand et al. (2018))

in 3DEC. (2) The permeability of the grain assembly was matched to that of intact granite matrix permeability by making the grains impermeable and allowing fluid flow only between grain contact. (3) SCDA-charged fracturing was simulated on the calibrated numerical assembly. (4) Hydraulic stimulation was mimicked on the intact grain assembly by considering compatible injection flow rates for the calibrated hydraulic apertures of the model.

SCDA-charged fracturing was simulated in this study using the method proposed by De Silva et al. (2023), where the physical expansion of SCDA was simulated using deformable blocks in an injection well. The expansion of the SCDA was capped by either a peak expansive pressure or a maximum strain, depending on which parameter was reached first in the simulation. For HS pre-conditioning, the typical extended leak-off test (XLOT) was adopted. The XLOT method is an extension of the standard leak-off test where the injection flow is sustained post-fracturing to ensure fracture growth (Hamidi and Mortazavi 2014). Therefore, in the simulations conducted, the injection flow rate was maintained beyond the initial breakdown pressure until continuous fracture extension was achieved in the model.

2.2 Hydro-mechanical Simulation of the Voronoi Grain Structure

Strathbogie granite was used as the reference material to calibrate the mechanical and hydraulic properties of the numerical grain assembly. Individual grains were modelled as an assembly of discrete Voronoi blocks with minimum and maximum edge lengths of 3 mm and 8 mm respectively. The grain sizes were selected to accurately represent material heterogeneity while being able to simulate fluid

flow with limited computational resources and time. Individual grains were internally meshed as finite difference elements consisting of tetrahedral zones with a zone edge length of 2 mm, allowing them to deform as linear elastic material with Young's modulus of E and Poisson's ratio of ν. Since 3DEC only supports parallel plate geometries for fluid flow calculations in joints, grain contacts are parallel in the Voronoi grain assembly. Contacts between grains were modelled using the Coulomb slip model allowing contacts to fail under both shear and tension (Fig. 3a). The shear strength of the joint is governed by contact cohesion c and the friction angle φ. Tensile failure is simulated by defining a tensile cut-off, σ_t between contacts. The shear and normal stiffnesses, k_s and k_n govern the displacement between joints and the joint apertures during mechanical deformation in coupled hydro-mechanical simulations.

A crack is formed between grains when the applied stresses exceed the tensile or shear capacity of the bond. Joint apertures vary depending on the mechanical loading and the fluid flow through grain contacts evolve with the mechanical loading of the model. As shown in Fig. 3b, grain contact apertures vary linearly depending on the applied stress and fluid pressure. The cubic law, given by Eq. (2) is used to calculate the flow q, through contact planes in the numerical model. The fluid flow is restricted to grain contacts only, enabling non-linear pressure dependence of joint apertures. The fluid simulations were run under the small-strain condition, which assumes grain positions and grid points are not changed during the simulation. This condition inhibits significant deformations between grain boundaries and allows the application of the cubic law by considering grain boundaries as parallel plates. Therefore, a fully coupled hydro-mechanical model in 3DEC requires meshing to be done internally as flow planes are superimposed on mechanical contact planes. Due to computational limitations, only intergranular fracturing was simulated in this study to achieve results within a practical timeframe.

$$q = \frac{a^3}{12\mu} \frac{\Delta p}{l} \qquad (2)$$

In Eq. (2), a is the hydraulic aperture, Δp is the fluid pressure drop along the selected boundary, l is the boundary length, and μ is the fluid viscosity. For flow calculations, the hydraulic aperture is assumed to be equal to the mechanical aperture and the average aperture between contact planes is used for flow calculations for non-parallel contact planes. The fluid pressures, p are updated based on net flow into the domain and volume change due to the deformation of grain boundaries and joints according to Eq. (3). Readers are directed to 3DEC documentation for an in-depth description of fluid flow simulations in joints (Itasca 2022).
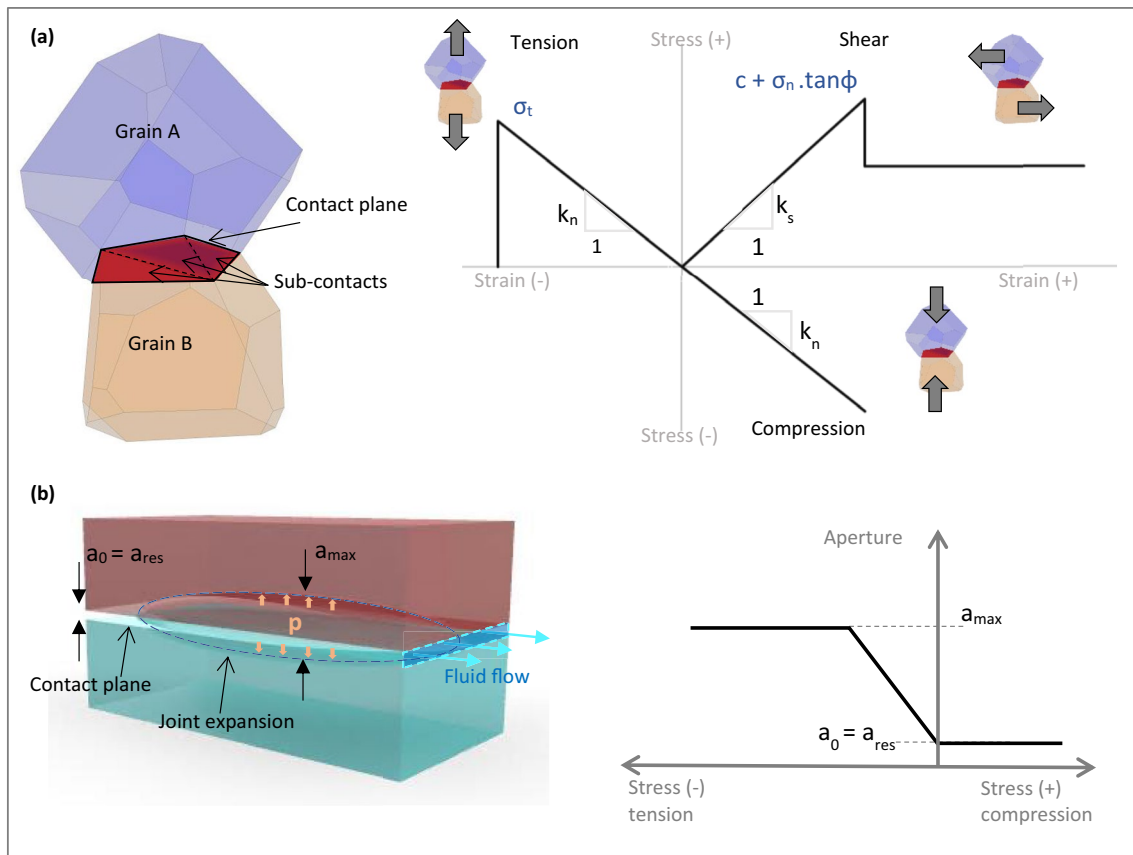
Fig. 3 Joint contact model **a** Coulomb slip model between contact planes of two grains, and **b** hydraulic aperture variation in contact (modified after Zhang and Dontsov 2018)

$$p = p_0 + \frac{K_w Q \Delta t}{V} - \frac{K_w \Delta V}{(V + V_0)/2} \qquad (3)$$

In Eq. (3), p_0 is the initial fluid pressure, K_w is the fluid bulk modulus, Q is the net flow rate into the domain, and V is the volume. $V = V_0 + \Delta V$, where ΔV is the volume change in the volume change in the domain at time Δt, and V_0 is the previous volume in the domain.

Upper and lower limits are imposed on the hydraulic aperture, used for the calculation of the fluid flow (Fig. 3b) so that the cubic law stands valid in the model. The upper limit is imposed to avoid turbulent flow regimes and the lower limit is imposed to account for non-zero joint apertures in real life. The residual aperture, a_{res} permits a minute fluid flow through contacts that can be calibrated to simulate the intrinsic matrix permeability of the intact material (i.e., leak-off).

2.3 HS Laboratory Experiment

Past research has shown that the direction of hydraulic fracture propagation originating from a central injection well is directly influenced by the initial principal stress state of the rock mass (Zeng et al. 2018). Material heterogeneity also influences the direction of fracture initiation around an injection well where the fractures orient in the direction of planes with the least fracture toughness (Sesetty and Ghassemi 2018). The existence of fissures has also been shown to increase the possibility of crack branching during pre-conditioning using HS (Taleghani 2010). The fluid viscosity influences the fracturing mode where low-viscosity fracture fluids were found to initiate intergranular (IG) fracturing (Chen et al. 2015).

A laboratory-scale hydraulic stimulation experiment was conducted on Strathbogie granite (see Table 1 for petrographic and mechanical properties of the specimen) to assess the nature of the induced fractures. A 22.5 mm diameter cylindrical test specimen was cored from an undamaged granite block. The specimen ends were finished using a diamond face grinder to produce a level and smooth surfaces with minimum surface irregularities (< 10 μm). A 3-mm hole was drilled into the center of the specimen for fluid injection. A schematic of the experimental setup and the boundary conditions used for hydraulic stimulation is shown in Fig. 4 and water was injected into the drilled borehole at a constant rate to initiate a hydraulic fracture. The readers are

Table 1 Petrographic and mechanical properties of granite

Property	Value %
Mineral distribution (by weight)	
Quartz	50.00
Orthoclase	13.00
Sodic and intermediate Plagioclase	16.00
Biotite—phlogopite	15.00
Other (Muscovite, Clinochlore, Dolomite)	6.00
Physical properties	
Bulk density, kg/m³	2630.00
Porosity, %	1.20
Mechanical properties	
Young's modulus, GPa[a]	17.13
Poisson's ratio[a]	0.24
Uniaxial compressive strength (UCS), MPa	120.94
Brazilian tensile strength (BTS), MPa	6.38

[a]Elastic properties were calculated using cylindrical specimens with 22.5 mm diameter and 45 mm height

directed to Kumari et al. (2018) for a detailed description of the experimental procedure.

3 Numerical Model Assembly and Calibration

3.1 Calibration of Mechanical Properties

The heterogeneity of Strathbogie granite was introduced to the model by considering varying mineralogical strength properties of grains and different grain contacts. Table 1 shows the experimentally observed petrographic and mechanical properties of granite.

For numerical simulations, the mineralogy in Table 1 was simplified to quartz, feldspar and mica representing the dominant mineral phases in the numerical assembly.

The mineralogy was randomly assigned to individual grains until the target percentages were achieved by the volume of the material using the Random Distribution of Properties (RDP) method (Wang et al. 2022a). Table 2 shows the volume percentage, calibrated elastic properties of individual grains and the different contact properties used to simulate interparticle bonds in the model. These micro-mechanical parameters for the grains and grain contacts were assigned by considering a Weibull random distribution given by Eq. (4).

$$F(x; \lambda, k) = \begin{cases} 1 - e^{-\left(\frac{x}{\lambda}\right)^k} & x \geq 0 \\ 0 & x < 0 \end{cases} \tag{4}$$

In Eq. (4), x is the Weibull distributed random variable, λ ($\lambda = 1$) is the scale parameter and k ($k = 7$) is the shape parameter.

The numerical model was calibrated by adjusting the micro-mechanical properties until the macro-mechanical responses for the Uniaxial Compressive Strength (UCS) and the Brazilian Disk tensile Strength (BTS) tests of the numerical model matched that of the granite specimens. The BTS σ_t was calculated using Eq. (5).

$$\sigma_t = \frac{2P}{\pi DT} \tag{5}$$

In Eq. (5), P is the peak diametrical load, and D and T are the diameter and the thickness of the specimen respectively.

A comparison between the experimental results and the numerical simulations of the calibrated model for the mechanical response of granite is shown in Table 3 and Fig. 5. The calibrated model was verified by calculating the fracture toughness K_{IC} of the material (Eq. 6) using a Notched Semi-Circular Bending (NSCB) test (Kuruppu et al. 2014).

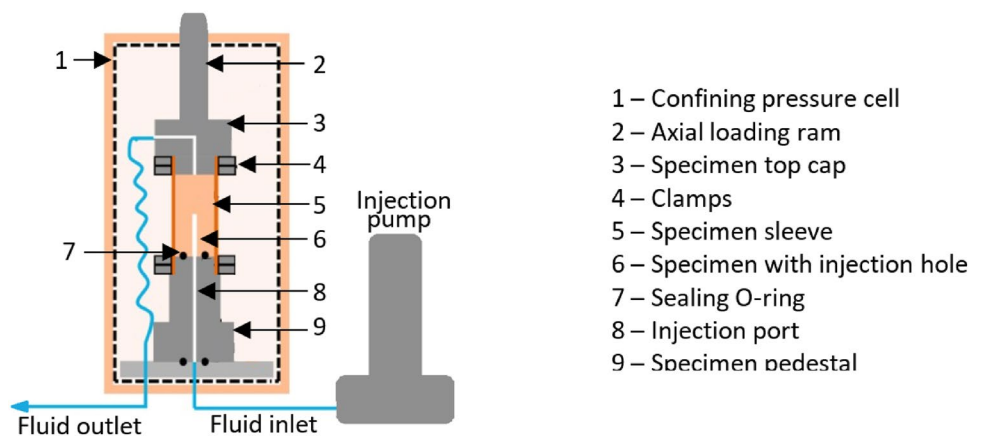**Fig. 4** Schematic diagram of the experimental setup for hydraulic stimulation

1 – Confining pressure cell
2 – Axial loading ram
3 – Specimen top cap
4 – Clamps
5 – Specimen sleeve
6 – Specimen with injection hole
7 – Sealing O-ring
8 – Injection port
9 – Specimen pedestal

Injection pump

Fluid outlet   Fluid inlet

Table 2 Calibrated micro-mechanical properties of the numerical assembly

Block properties

Mineral	Density (kg/m^3)	Young's modulus (GPa)	Poisson's ratio	Volume percentage (%)
Mica (M)	3050.00	11.73	0.29	16.34
Feldspar (F)	2620.00	15.64	0.25	32.68
Quartz (Q)	2650.00	27.37	0.21	50.98

Contact properties

Interface	k_n (GPa/m)	k_s (GPa/m)	φ (°)	c (MPa)	σ_T (MPa)
M–M	79,475.00	15,130.00	20.25	43.16	11.20
F–F	113,900.00	21,675.00	33.75	49.80	14.56
Q–Q	185,300.00	35,105.00	40.50	56.44	17.92
M–F	$(k_{n,M}+k_{n,F})/2$	$(k_{s,M}+k_{s,F})/2$	$(\varphi_{,M}+\varphi_{,F})/2$	$(c_{,M}+c_{,F})/2$	$(\sigma_{T,M}+\sigma_{T,F})/2$
M–Q	$(k_{n,M}+k_{n,Q})/2$	$(k_{s,M}+k_{s,Q})/2$	$(\varphi_{,M}+\varphi_{,Q})/2$	$(c_{,M}+c_{,Q})/2$	$(\sigma_{T,M}+\sigma_{T,Q})/2$
F–Q	$(k_{n,F}+k_{n,Q})/2$	$(k_{s,F}+k_{s,Q})/2$	$(\varphi_{,F}+\varphi_{,Q})/2$	$(c_{,F}+c_{,Q})/2$	$(\sigma_{T,F}+\sigma_{T,Q})/2$

Table 3 Mechanical response of Strathbogie granite, a comparison between laboratory experiments and numerical simulations

Parameter	Laboratory test result	Numerical simulation	Error %	Specimen dimensions (mm)				
				D**	H**	T**	A**	S**
UCS (MPa)	120.94^	114.46	5.11	22.50	45.00	–	–	–
BTS (MPa)	6.38*	6.34	0.63	38.00	–	19.00	–	–
K_{IC}, NSCB (MPa m$^{1/2}$)	1.35#	1.40	3.70	50.00	–	20.00	8.33	40.00
E (GPa)	17.13^	17.27	0.82					
ν	0.24^	0.23	4.16					

*Averaged form Kumari et al. (2019), ^Kumari et al. (2017), #averaged from Yin et al. (2020), **D, H, T, A, and S correspond to diameter, height, thickness, notch length, and NCSB specimen support spacing respectively

$$K_{IC} = Y' \frac{P\sqrt{\pi A}}{DT} \tag{6}$$

In Eq. (6), P is the peak bending load, A is the notch length at the center of the specimen, and $Y\prime$ is given by Eq. (7).

$$Y' = -1.297 + 9.516\left(\frac{s}{2R}\right) - \left(0.47 + 16.457\left(\frac{s}{2R}\right)\right)\frac{2A}{D}$$
$$+ \left(1.071 + 34.401\left(\frac{s}{2R}\right)\right)\left(\frac{2A}{D}\right)^2 \tag{7}$$

3.2 Calibration of Intact Rock Permeability

Following the calibration of the macro-mechanical properties of the rock, the permeability of the intact matrix was calibrated considering different residual joint apertures in the model as previously discussed. The residual joint aperture a_{res} (Fig. 3b) was changed in the model and the matrix permeability was calculated using constant head permeability tests. The permeability, k of the matrix was calculated using Eq. (8).

$$k = \frac{Q\mu H}{A\Delta P} \tag{8}$$

where Q is the cumulative steady-state flow rate observed at the injection point normal to the specimen cross-sectional area A, and $\Delta P/H$ is the pressure gradient. Model dimensions and boundary parameters used in this simulation are identical to those used by Kumari et al. (2018) to measure the intrinsic permeability of Strathbogie granite. The model parameters used and the average flowrate $\bar{q}$ observed in the flow planes at the injection plane for the selected parameters are shown in Table 4. The fluid pressure and the flow rate distributions of the specimen at a steady state are shown in Fig. 6a and b, respectively. The steady state was achieved by running the model until the pore pressures stabilized
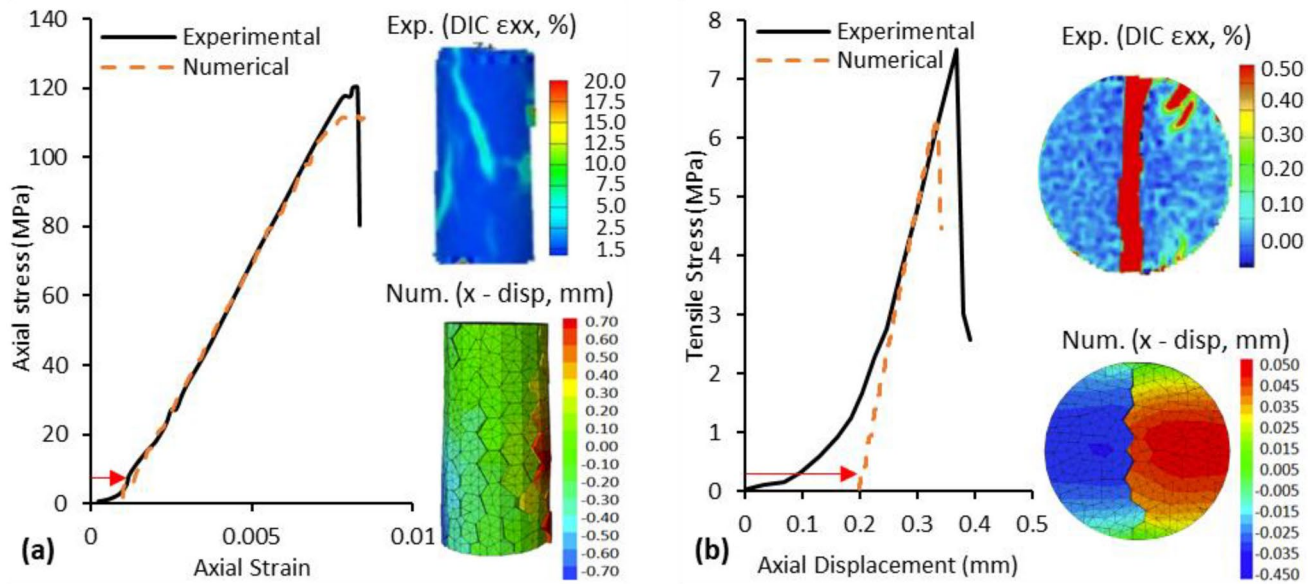
Fig. 5 Stress–strain response comparison of the numerical model **a** UCS, and **b** BTS. The numerical result is shifted in the *x*-axis to align with the experimental results as indicated by the arrow. Point strain within the specimen (Fig. 6c). The cumulative flow rate *Q*, measurements obtained by digital image correlation (DIC), indicate axial splitting for the UCS specimen (Kumari et al. 2017) and diametrical splitting for the BTS specimen (Kumari et al. 2019)

in this simulation corresponds to the summation of flow-rates through flow planes between grain boundaries at the injection face as indicated by red line segments in Fig. 6b ($Q_{in} = \sum q_i l_i = \overline{q}L$). q_i, the flowrate per unit width is calculated using Eq. (2). A similar methodology was adopted by Tan and Konietzky (2019) to simulate the intact permeability of Granite in 2D. Figure 6d shows the variation of the specimen permeability with grain contact plane aperture a_0 which indicates a non-linear variation. Considering the experimental permeability of intact Strathbogie granite of 1.00×10^{-19} m^2 at 10 MPa confining pressure (Kumari et al. 2018), a_0 of 2×10^{-7} m yielded a reasonable result.

4 Fracture Simulations in 3DEC

4.1 SCDA Charging and Hydraulic Fracture Numerical Simulation

SCDA is typically introduced into a rock mass as an injectable slurry through pre-drilled boreholes. Once, injected, the SCDA transforms into a solid state during the hydration process and results in the volumetric expansion explained in Sect. 1.4. The elastic properties of SCDA evolve with the hydration of SCDA (De Silva et al. 2017; Xu et al. 2021) and the stiffness of the SCDA influences the expansive pressure exerted on the injection well boundary (Tang et al. 2022). However, the numerical model in this study simulates SCDA expansion from the point of transition to a solid state, and constant material properties were assumed for simulating the solid SCDA in the numerical model (Table 5).

The expansion of SCDA was modelled by generating a uniform radial distribution of tetrahedral expansive elements within the borehole. Experimental observations of SCDA expansion yield an exponential decay of the strain rate applied by SCDA on the surrounding material (De Silva et al. 2023). This can be translated into a normal velocity boundary in SCDA elements for implementation in 3DEC that follows the decay function given by Eq. (9).

$$v = f \cdot e^{-bt} \qquad (9)$$

where, *v* is the velocity magnitude, *f* and *b* are shape factors governing the rate of expansion in SCDA and *t* is the total simulation time in 3DEC. SCDA-charged fracture propagation was terminated in the model in one of two ways; either by *v* asymptotically reaching zero as the simulation progresses (corresponding to the finite strain energy in SCDA expansion) or when the expansive pressure in the model reaches a predefined peak value based on experimental data. In this simulation, for the calibrated rock mass, the peak expansive pressure was limited to 45 MPa, *f* = 1 and *b* = 20 in Eq. (9). For further details of the simulation method, readers are directed to De Silva et al. (2023).

In the coupled numerical model presented, the grain boundaries can open and slip as a function of effective stress and their bond strength. A fracture is registered between two contacts (grain boundaries) when the tensile or shear strength of the bond is exceeded as a result of block

Table 4 Model parameters used for the calibrated intact rock matrix flow

P_{in}	P_{out}	A	H	μ	L	$\bar{q}$	a_0	a_{max}
8 MPa	0 MPa	3.98×10^{-4} m^2	0.045 m	1×10^{-3} Pa.s	0.145 m	1.45×10^{-11} m^2	2×10^{-7} m	3×10^{-5} m

deformation and/or pore-pressure build-up in the contact during fluid injection. Hydraulic fracturing is simulated by applying a constant flowrate injection boundary to a predefined injection well in the model (See Sect. 4.3). During the fracture simulations, the bonds between grains are allowed to progressively fail representing hydraulic fracture propagation. As the fractures propagate, the pore pressure dissipation within the fluid planes is simulated with the coupled hydro-mechanical simulations (as explained in Eq. 3). Since the grain assembly represents a heterogeneous material, in addition to the initial stress state of the model, the fracture evolution is also dictated by the varying bond strength between different grain contact boundaries.

4.2 HS Model Verification in 3DEC

An initial model was run to verify the validity of planar hydraulic fracture propagation in 3DEC. The closed-form theoretical approximation for the fracture aperture and pressure variation along the fracture plane of a radially growing penny-shaped hydraulic fracture (Fig. 7) in an isotropic elastic medium was considered for the validation (Dontsov 2016; Savitski and Detournay 2002). The solution is only valid under the following assumptions.

1. Incompressible Newtonian fluid injection from a point source at the center of the fracture
2. The lag between the fluid front and the fracture tip during fracture propagation is negligible
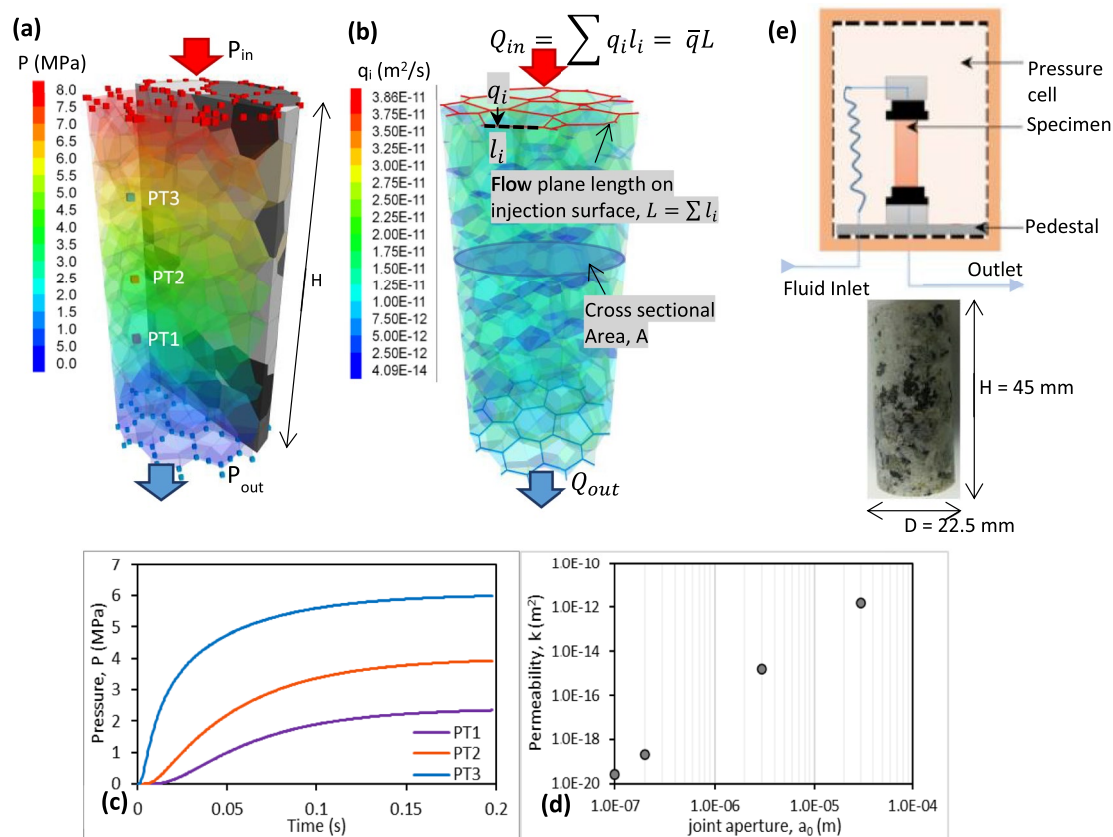

Fig. 6 Steady state constant head permeability test for intact rock **a** numerical assembly and the pressure distribution with pressure measurement points PT1–PT3, **b** flowrate distribution within grain contacts during steady state (inflow and outflow pressure boundaries denoted by red and blue points respectively), **c** pressure stabilization within grain assembly (steady state flow) for points PT1–PT3, **d** the variation of permeability within the grain assembly with different contact apertures, and **e** schematic of the experimental setup and the specimen used to calculate the matrix permeability (Kumari et al. 2018)

Table 5 Micro-mechanical properties of SCDA in 3DEC

Block properties		
Density (kg/m³)	Young's modulus (GPa)	Poisson's ratio
2600	57.00	0.22

Contact properties				
k_n (GPa/m)	k_s (GPa/m)	φ	C (MPa)	σ_T (MPa)
217,600.00	41,344.00	30.00	68.00	16.00

Fig. 7 Penny-shaped hydraulic fracture propagation (Savitski and Detournay 2002)
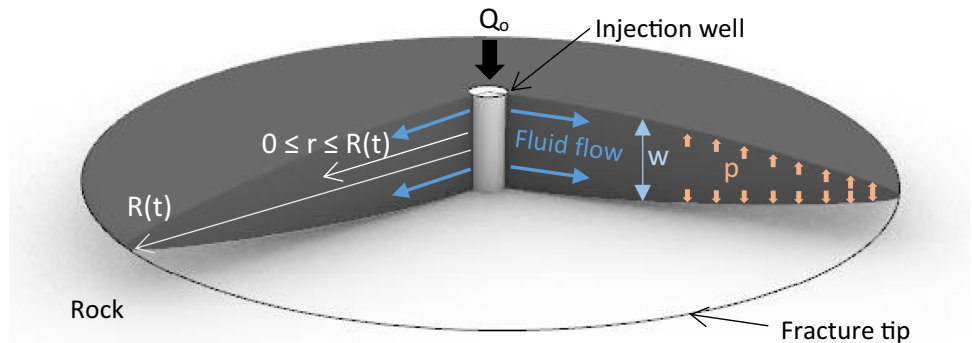
3. Continuous fracture propagation in mobile equilibrium
4. Lubrication theory is applicable, $\partial p/\partial w = 0$, where p is the fluid pressure and w is the crack aperture

The fracture propagation of a Penny-shaped fracture is dependent on the fluid viscosity μ, Material Young's modulus E, fracture toughness K_{IC} and fluid leak-off parameter, C, which have been introduced in the scaled form for convenience (Eq. 10) (Savitski and Detournay 2002).

$$\mu' = 12\mu, \; E' = \frac{E}{1-v^2}, \; K' = 4\left(\frac{2}{\pi}\right)^{0.5} K_{IC}, \; C' = 2C \quad (10)$$

Under zero fluid leak-off, fracture propagation is categorized as either in toughness-dominated (K) or viscosity-dominated (M) regime (Dontsov 2016). The limiting regime (for $C = 0$ case) is determined by the dominance of the dissipative mechanism associated with either fluid viscosity or rock toughness during fracture propagation. The M vertex limit corresponds to a viscosity dominated and zero toughness ($K_{IC} = 0$) condition, indicating zero (tensile and shear) strength in the hydraulic fracture. Therefore, hydraulic fracture propagation in an isotropic elastic medium as shown in Fig. 7 can be described by:

$$w\left(\frac{r}{R}, t\right) = 1.1901\left(\frac{\mu'^2 Q_o^3 t}{E'^2}\right)^{\frac{1}{9}}\left(1 + \frac{r}{R}\right)^{0.487}\left(1 - \frac{r}{R}\right)^{\frac{2}{3}}$$

$$(11)$$

$$p\left(\frac{r}{R}, t\right) = 2.4019\left(\frac{\mu' E'^2}{t}\right)^{\frac{1}{3}} F\left(\frac{r}{R}, 0.487, \frac{2}{3}\right) \quad (12)$$

$$R(t) = 0.6944\left(\frac{Q_o^3 E' t^4}{\mu'}\right)^{\frac{1}{9}} \quad (13)$$

where Q_o is the injection flow rate, w is the fracture aperture, and p is the pressure gradient along the fracture radius R, at a given time t (See Fig. 7). F is defined as an integral containing a piecewise function, defined as

$$F\left(\rho, \lambda, \bar{\delta}\right) = \frac{1}{2^{1+\lambda}\pi}\int_0^1 \frac{\partial M(\rho, s)}{\partial s}(1-s)^\lambda (1-s)^{\frac{2}{3}}ds \quad (14)$$

where, $\rho = r/R$, $s = 1-\rho$ and the piecewise function $M(\rho, s)$ is defined as

$$M(\rho, s) = \begin{cases} \frac{1}{\rho}K\left(\frac{s^2}{\rho^2}\right) + \frac{\rho}{s^2-\rho^2}E\left(\frac{s^2}{\rho^2}\right), \rho > s \\ \frac{s}{s^2-\rho^2}E\left(\frac{s^2}{\rho^2}\right), \rho < s \end{cases} \quad (15)$$

In Eq. (15), $K(\cdot)$ and $E(\cdot)$ are complete elliptic integrals of the first and second kind respectively. For the M vertex solution, $\lambda \sim 0.487$, and $\bar{\delta} \sim 2/3$ (Dontsov 2016). The asymptotic solution for Eqs. (11 and 12) is numerically
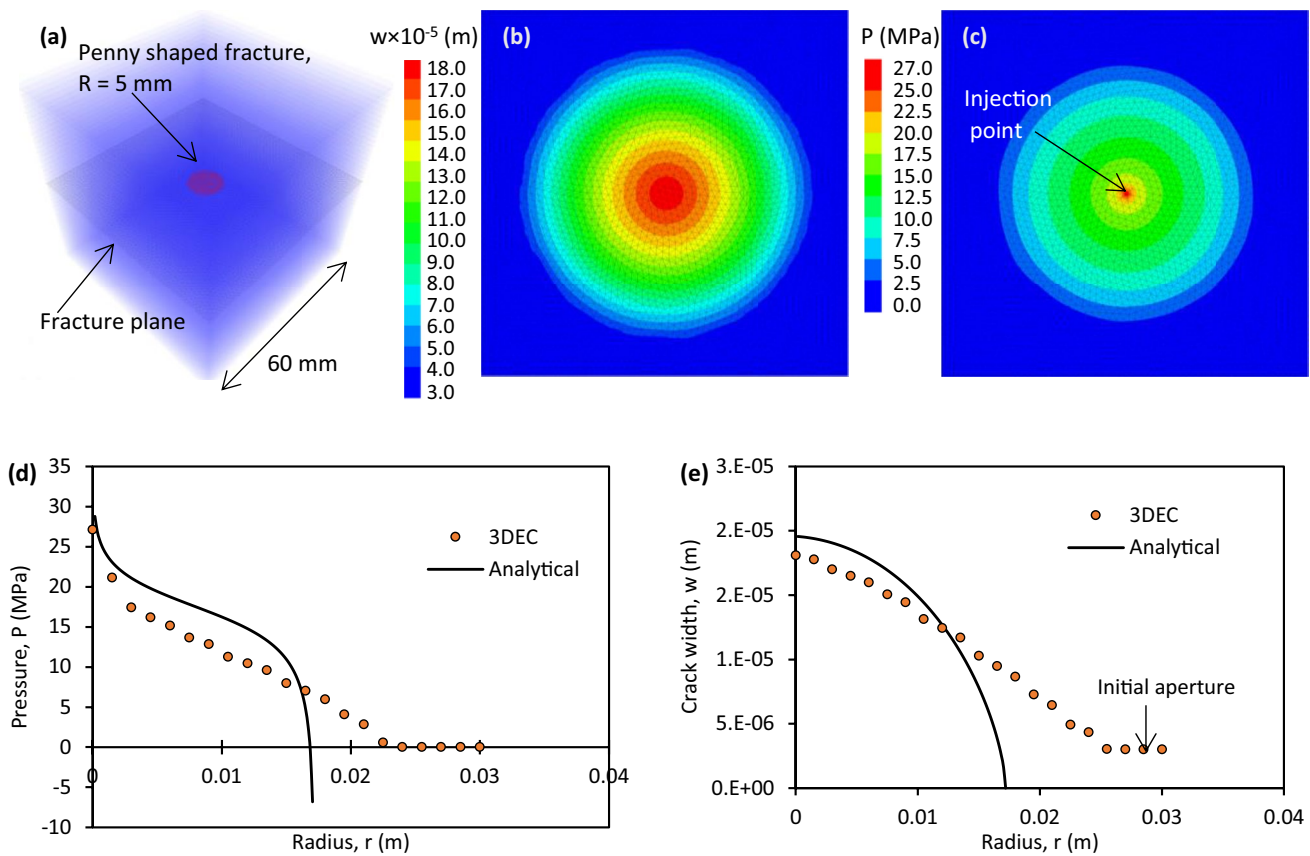
Fig. 8 Comparison of analytical and numerical results for a penny-shaped hydraulic fracture propagation at $t = 10^{-3}$ s. **a** Initial numerical model, **b** hydraulic aperture contour c fluid pressure contour, and the variation of **d** crack width (aperture) and **e** pressure along the fracture radius

approximated by Eqs. (16 and 17) (Zolfaghari and Bunger 2019).

$$w = 0.6955 \left[\begin{array}{l} 1.9093(1 - \rho)^{\frac{2}{3}} + 0.0705(13\rho - 6)s^{\frac{2}{3}} \\ + 0.236\sqrt{(1 - \rho^2)} - \rho \cos^{-1} \rho \end{array} \right] \left(\frac{Q_o^3 \mu'^2}{E'^2} \right)^{\frac{1}{9}} t^{\frac{1}{9}}$$

(16)

$$p = \left(0.8593 - \frac{0.2387}{s^{\frac{2}{3}}} - 0.09269 \ln \rho \right) \left(\mu' E'^2 \right)^{\frac{1}{3}} t^{-\frac{1}{3}}$$ (17)

A 60 mm cube with a horizontal penny-shaped crack with a 10 mm diameter and zero tensile strength and cohesion was modelled with a single injection point with a flow rate $Q_o = 10^{-5}$ m³/s in 3DEC to replicate the analytical solution. Young's modulus, E of 40 MPa, Poisson's ratio, ν of 0.22 and fluid viscosity, μ of 0.001 Pa s was considered for the model. An initial (and minimum) hydraulic aperture of 3×10^{-6} m and a maximum hydraulic aperture of 10^{-4} m was defined for fluid flow through fractures. To simulate zero leak-off, fluid flow was permitted only in failed contacts in this instance. The analytical solution was compared against the numerical results at $t = 10^{-3}$ s after starting the fluid injection.

Figure 8 shows the initial model and the observed pressure and fracture aperture distribution comparison with the analytical solution at the end of 10^{-3} s. The model simulates the outward propagation of the fracture with reasonable accuracy. Although there is a deviation at the crack tip, this can be attributed to the non-zero initial fracture aperture and the finite bulk modulus (compressible fluid) defined in 3DEC. These were assumed to be zero aperture at the crack tip and incompressible fluid in the analytical solution.

4.3 The Hybrid SCDA-HS Method in the Granular Assembly

In this study, first SCDA charging was simulated to initiate multiple radial fractures around a central injection well followed by a constant rate fluid injection applied to the boundary nodes of the injection well. The boundary conditions and the model geometry used to simulate the hybrid SCDA-HS pre-conditioning method are shown in Fig. 9.
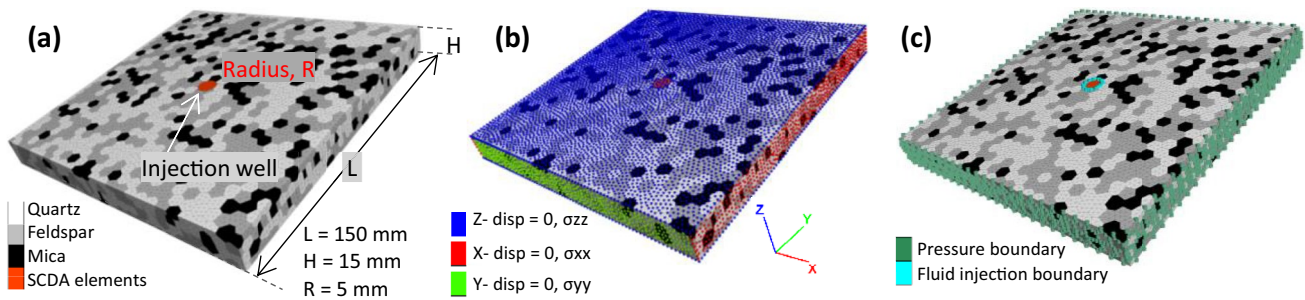
Fig. 9 Model boundary conditions, **a** heterogeneous grain assembly and SCDA expansion elements, **b** stress boundary conditions, and **c** fluid boundary conditions with permeable boundaries at edges and flow boundary at the injection well

No fluid flow was permitted through the top and bottom surfaces of the boundary.

5 Results and Discussion

5.1 SCDA Pre-conditioning

Previous research has shown that the in-situ stress conditions (De Silva et al. 2018b; Guo et al. 2015; Zhai et al. 2018) and material properties strongly influence the fracture initiation pattern of SCDA charging (Lei et al. 2021). In this study, the effects of stress anisotropy and increasing confining pressure on the overall fracture initiation, growth and termination in heterogeneous rock were investigated first. Figure 10 shows the SCDA-charged fracture pattern observed for four different stress regimes shown in Table 6. The stress regimes in Table 6 were used for all subsequent simulations. A comparison of Case 1 and Case 3 exhibits the influence of isotropic confining pressure in the *XY* plane, while Case 2 and Case 3 exhibit the effect of stress anisotropy on SCDA-charged fracturing. Finally, a comparison of Case 2 and Case 4 reveals how the increased intensity of stress anisotropy influences fracture propagation.

The tangential stresses developed around the injection well during SCDA charging are shown in Fig. 10 (compression is considered positive). Figures 10a–d show the variation of the tangential tensile stress developed around the injection well at fracture growth termination for the four stress conditions considered. The results indicate fracture termination within the tangential tensile stress field. It is evident, that at lower confining pressures (Case 1) the tensile stress field reaches further outward from the injection well, contributing to extended radial fractures, whereas increasing the confinement (Case 3) appears to restrain the extension of

SCDA-charged fracturing. This phenomenon can be better explained by observing the evolution of the average tangential stress around the injection well (Fig. 10e). The initial tangential stress around the injection well is compressive (positive) due to the in-situ stress state. Next, the tangential tensile stress created by SCDA expansion in the borehole results in the reorientation of stresses around the injection well. In other words, the stress reorientation transforms the near-borehole tangential stress from a compressive state to a tensile state (state 1 in Fig. 10e). Fracture initiation is inhibited until this tensile stress exceeds the tensile strength between mineral grains (state 2, in Fig. 10e) and the initiated fractures continue to grow within the tensile stress field (state 3, in Fig. 10e).

As the in-situ stress increases, the energy spent by SCDA expansion for stress reorientation in state 1 increases. Therefore, a reduction in the energy spent on fracture extension is expected leading to shorter fracture lengths. Furthermore, the in-situ stress anisotropy skews the otherwise circular tensile stress state around the injection well as shown in Fig. 10b and d. However, the overall geometry of the SCDA-charged fracturing remains relatively unaffected by the in-situ stress distribution at lower stress ratios (Case 2). Comparing Fig. 10b and d shows that the increased stress anisotropy in the *XY* plane further skews the tensile stress field, contributing to fracture extension in the *Y* direction (higher stress) and crack growth suppression in the *X* direction.

5.2 HS Pre-conditioning

The hydraulic fracturing test was performed at unconfined conditions to achieve the best visibility of the generated fractures. However, a constant axial load of 2 kN was
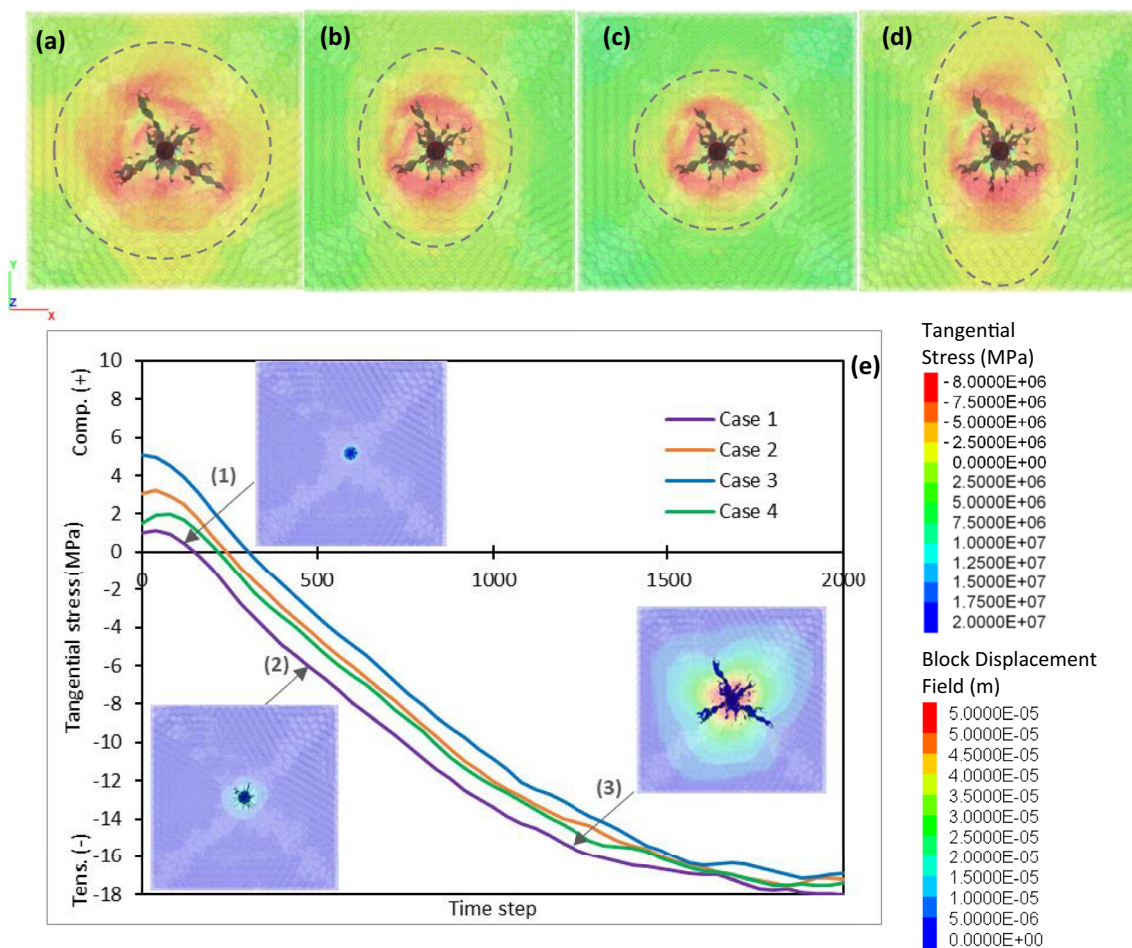
Fig. 10 Fracture pattern produced by SCDA charging and minor principal stress distribution (in MPa) at fracture growth termination for different stress **a** Case 1 ($\sigma_x = 1$ MPa, $\sigma_y = 1$ MPa), **b** Case 2 ($\sigma_x = 2.5$ MPa, $\sigma_y = 5$ MPa), **c** Case 3 ($\sigma_x = 5$ MPa, $\sigma_y = 5$ MPa), **d** Case 4 ($\sigma_x = 1$ MPa, $\sigma_y = 5$ MPa), and **e** minor principal stress evolu-

tion during the SCDA charging process where (1) is the stress reorientation state, (2) is fracture initiation state and (3) is fracture growth state. The fracture pattern and the displacement field in m are shown for the three distinct states for Case 1

maintained during the experiment ensuring a greater axial stress (~ 5 MPa) on the specimen compared to the lateral stress (0 MPa) to facilitate crack growth in the vertical direction. A fluid injection rate of 5 ml/min was maintained during the experiment and the breakdown pressure was observed at 9.16 MPa. The X-ray CT reconstruction of the observed fracture pattern is shown in Fig. 11a. As seen in the CT image reconstruction, a single diametrical fracture was

observed. Given the similar densities of feldspars and quartz, distinguishing these minerals from the CT images is difficult. However, a clear demarcation was observed between mica (lighter spots) and the rest of the rock matrix. Comparing mica boundaries in the fracture path, it is evident that the fracture path mainly follows grain boundaries. Therefore, the IG cracking simulated in the numerical assembly presented in this study would yield a realistic result in terms of the crack path.

The limitations of the small-strain conditions and the maximum apertures of the numerical model suggests, it is more suited to simulate confined rock and may be unrealistic to simulate large deformations observed during HS in unconfined conditions. However, a realistic prediction of the breakdown pressure can be obtained through the simulation process presented (Fig. 11b). By simulating identical conditions to the HS experiment, a comparable fracture pattern and a breakdown pressure of 8.39 MPa (8.35% error) were

Table 6 In-situ stress states

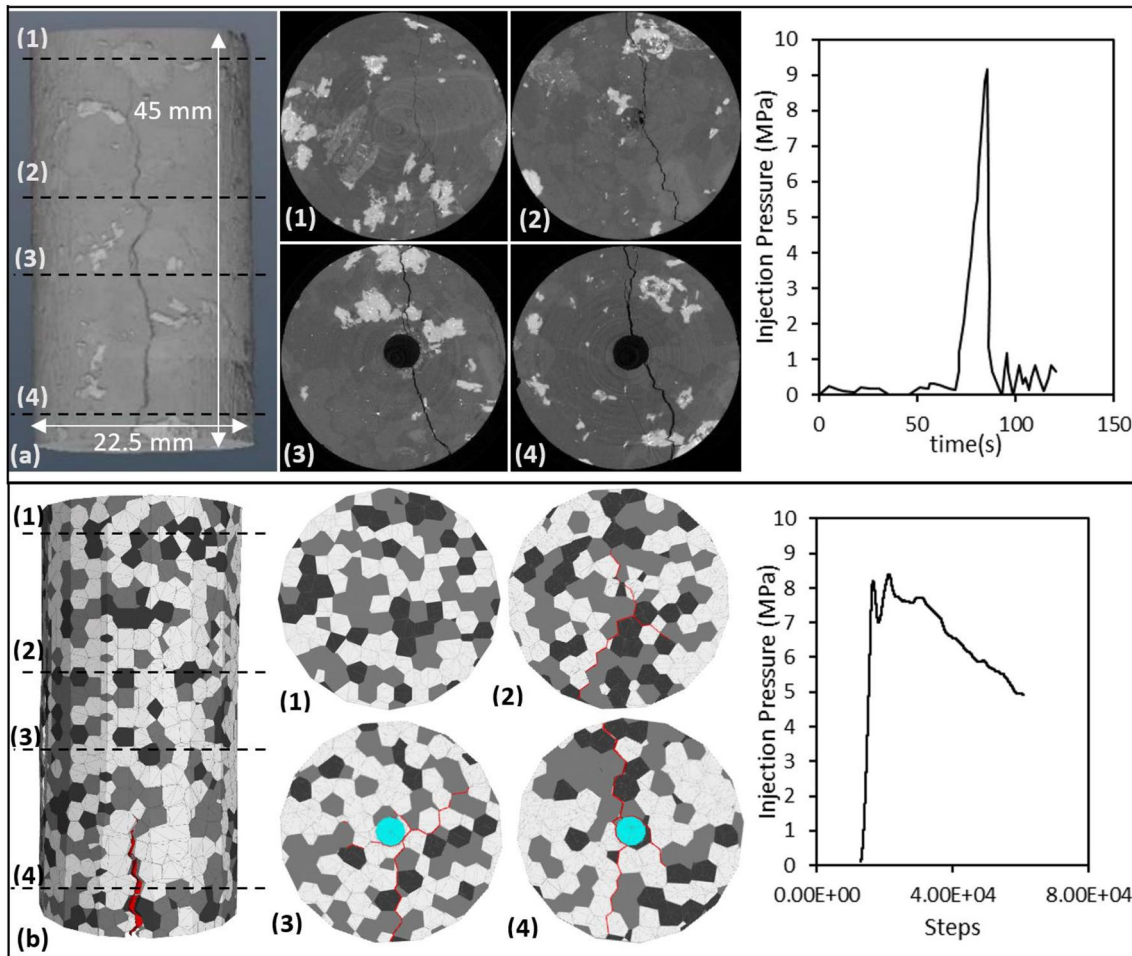| Case	X (MPa)	Y (MPa)	Z (MPa)	Stress ratio (XY plane)
1	1.00	1.00	1.00	1.0
2	2.50	5.00	1.00	2.0
3	5.00	5.00	1.00	1.0
4	1.00	5.00	1.00	5.0

Fig. 11 Hydraulic stimulation. **a** CT scanned Granite specimen after hydraulic stimulation under unconfined conditions, and **b** numerical simulation of the hydraulic fracture. Left, 3-dimensional reconstruc-tion of the diametrically split specimen. Center, cross sections depict-ing the observed fracture pattern across the specimen. Right, Injec-tion and breakdown pressure

observed. This error can be attributed to several factors such as the grain size used in the model, fluid leak-off during the experiment, and the compressibility of the fluid.

5.3 Effect of Stress Anisotropy and Heterogeneity on HS Fracture Propagation

Figure 12 shows the fracture patterns observed in the gran-ular assemblies for the in-situ stress conditions given in Table 6 at a fluid injection rate of 18 ml/min. Compared to SCDA charging, HS produced a single fracture that reached the specimen boundary, which was driven by the fluid pres-sure at the fracture tip irrespective of the in-situ stress field. At a stress ratio of 1 (Case 1: $\sigma_x = \sigma_y = 1.0$ MPa and Case 3: $\sigma_x = \sigma_y = 5.0$ MPa) in the XY plane, the fracture grew diagonally, which was dictated by the grain arrangement. Increasing the in-situ stress initiated additional minor crack-ing around the injection well (from 10,439 cracks in Case 1 to 11,377 cracks in Case 2: $\sigma_x = 2.5$ MPa, $\sigma_y = 5.0$ MPa) and

increased the tortuosity of the main fracture (Fig. 12a and c). The Tortuosity was calculated on the horizontal plane by considering the fracture length on the top face of the specimen. The geometric two-dimensional tortuosity was defined as the ratio of fracture length (geodesic length) and the straight line distance between the two ends of the frac-ture (Euclidean length) (Shanti et al. 2014).

Additionally, HS shows a higher sensitivity to the in-situ stress anisotropy compared to SCDA charging. At an XY plane stress ratio of 2 (Case 2), the HS fracture grows in the Y direction with some minor crack branching in the X direction (Fig. 12b), particularly around the injection well. This crack branching is suppressed when the stress ratio was further increased to 5 (Case 4). Furthermore, increasing the stress ratio in the XY plane from 1 to 5 (Fig. 12a, b, and d) exhibits an increase in the shearing effect of the fracture as indicated by the reduction of tensile to shear crack (T/S) ratios from 8.45 to 6.49. However, these additional shear
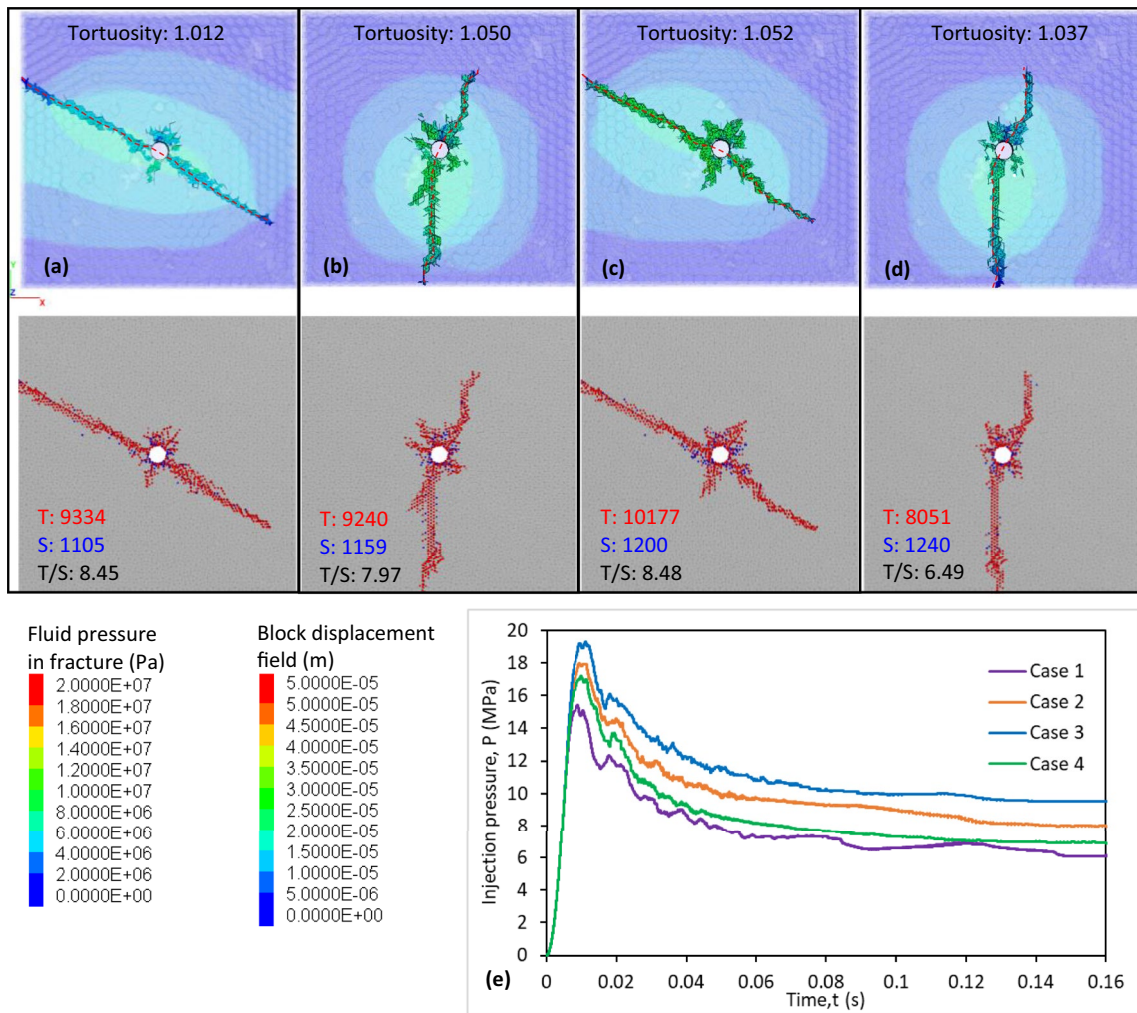
Fig. 12 Effect of confining pressure on the HS fracture pattern and tensile to shear crack ratio, in-situ stress **a** Case 1 ($\sigma_x = 1$ MPa, $\sigma_y = 1$ MPa), **b** Case 2 ($\sigma_x = 2.5$ MPa, $\sigma_y = 5$ MPa), **c** Case 3 ($\sigma_x = 5$ MPa, $\sigma_y = 5$ MPa), **d** Case 4 ($\sigma_x = 1$ MPa, $\sigma_y = 5$ MPa), and **e** fluid injection pressures for each case. The block displacement field (background color field) and the fluid pressure inside the failed contacts are shown at the top and the corresponding tensile (red) and shear (blue) cracks are shown at the bottom

and tensile cracks are primarily concentrated around the injection well.

The fluid pressure inside the injection well during the fracturing process for each case is shown in Fig. 12e. As expected, the highest breakdown pressure was recorded for the highest in-situ stress condition (Case 4) and the lowest breakdown pressure was recorded for the lowest in-situ stress state (Case 1). However, the slightly higher breakdown pressures for Case 2 and Case 3 correspond to additional cracking around the injection and the greater overall compressive stress in the X–Y plane. This phenomenon can be alleviated by inducing crack initiation points

around the injection well. However, comparing Case 2 and Case 4 indicates that although the breakdown pressures are relatively similar a significantly lower T/S ratio was observed for Case 4, indicating a strong influence of the stress anisotropy on the failure mode during HSs.

5.4 The Effect of Material Heterogeneity, Grain Size and Mineral Distribution on HS

Four different Voronoi grain distributions were considered to assess the influence of grain arrangement on fracture initiation and propagation. The grain size distributions
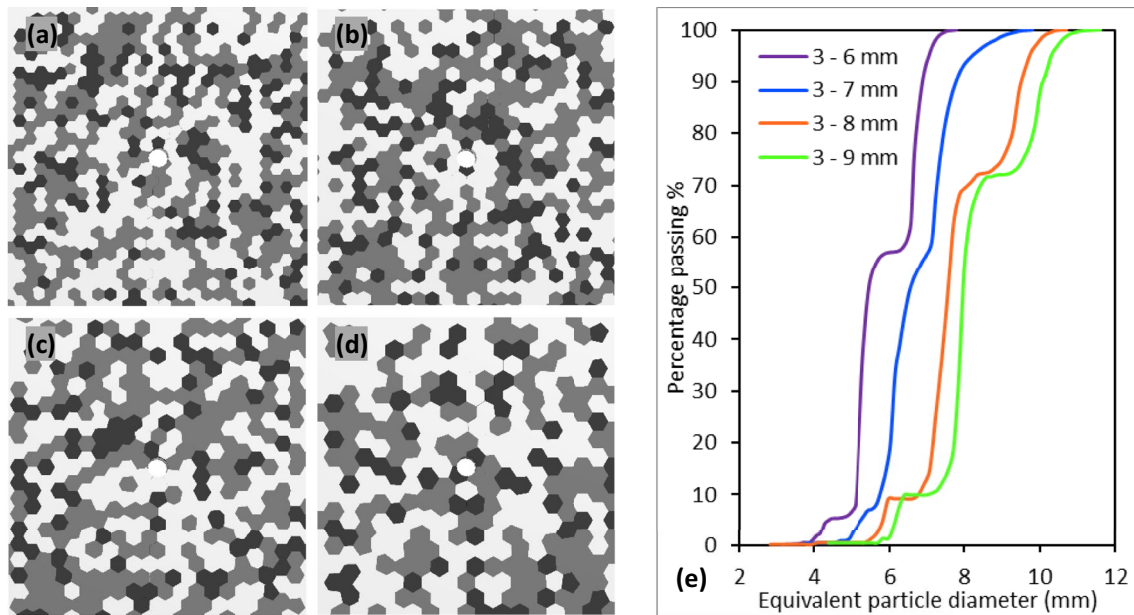
Fig. 13 Grain assemblies. The corresponding grain assemblies for minimum and maximum seed lengths for the four Voronoi distributions **a** 3–6 mm, **b** 3–7 mm, **c** 3–8 mm, **d** 3–9 mm, and **e** the equivalent particle size distributions

and the grain arrangements of the four models are shown in Fig. 13. The same mineralogy was used across the four assemblies (Table 2) and only the spatial distribution of the minerals was randomized. The minimum edge length for meshing the microstructure was kept constant at 1.4 mm for all four assemblies, which eliminated the influence of mesh size on fracture propagation.

The four assemblies were hydraulically fractured with an injection rate of 18 ml/min at the central injection well under Case 4 ($\sigma_x = 1.0$ MPa, $\sigma_y = 5.0$ MPa) in-situ stress condition. The observed fracture patterns, fluid leak-off into the matrix, and the different grain contacts that failed during the simulation are shown in Fig. 14a–d. Although the overall crack growth is in the Y direction (due to the stress anisotropy), the grain arrangement seems to influence both the fracture path and the extent of fluid leak-off into the rock matrix, despite maintaining identical injection rates and in-situ stress states. This is because the fluid flow during hydraulic stimulation follows the path of least resistance and the energy required to fail contacts depends on the adjoining mineral grain type (Table 2).

Figure 14e shows a comparison between the different contact types as a fraction of total (failed and intact) contacts in the entire assembly (denoted by T) and the contact types as a fraction of total failed contacts (denoted by C) for the four grain assemblies simulated. In other words, T includes both failed and intact contacts and C includes only failed contacts. The two most abundant contact types F–Q and Q–Q in the model show an indication of crack growth in the path of least resistance. As seen in Fig. 14e, an overall

increase in the fraction of F–Q contacts and a decrease in the fraction of Q–Q contacts were observed in the failed contacts. This is because F–Q contacts require lower energy to fail than Q–Q contacts, leading to fracture propagation with the least resistance. This relationship was less apparent in the other contact types due to the lower percentage of mica grains in the assemblies.

The fluid pressure development in the injection wells for the four assemblies considered is shown in Fig. 14f. Although the crack path showed dependence on the mineral distribution and the grain arrangement, the breakdown pressure showed little to no variation. This is because the macro-mechanical response of the four grain assemblies remained relatively unchanged since identical mineralogy and comparable grain-size distributions were considered for each of the four grain assemblies. The pressure distribution within the rock matrix due to fluid leak-off is also shown in Fig. 14a–d. This fluid leak-off pressure distribution reflected dependency on grain arrangement and it is fair to assume that pre-existing defects, particularly fissures in granitic rock can also influence the fracture pattern produced by hydraulic stimulation. Therefore, hydraulic stimulation in the presence of grain scale fissures (micro-cracks) was investigated next.

5.5 The Effect of Fissures on HS

Zhou et al. (2020) have shown two types of defects that can develop in granite micro-structure. The first is thermal cracks arising due to thermal expansion and different thermal coefficients between individual grains that form
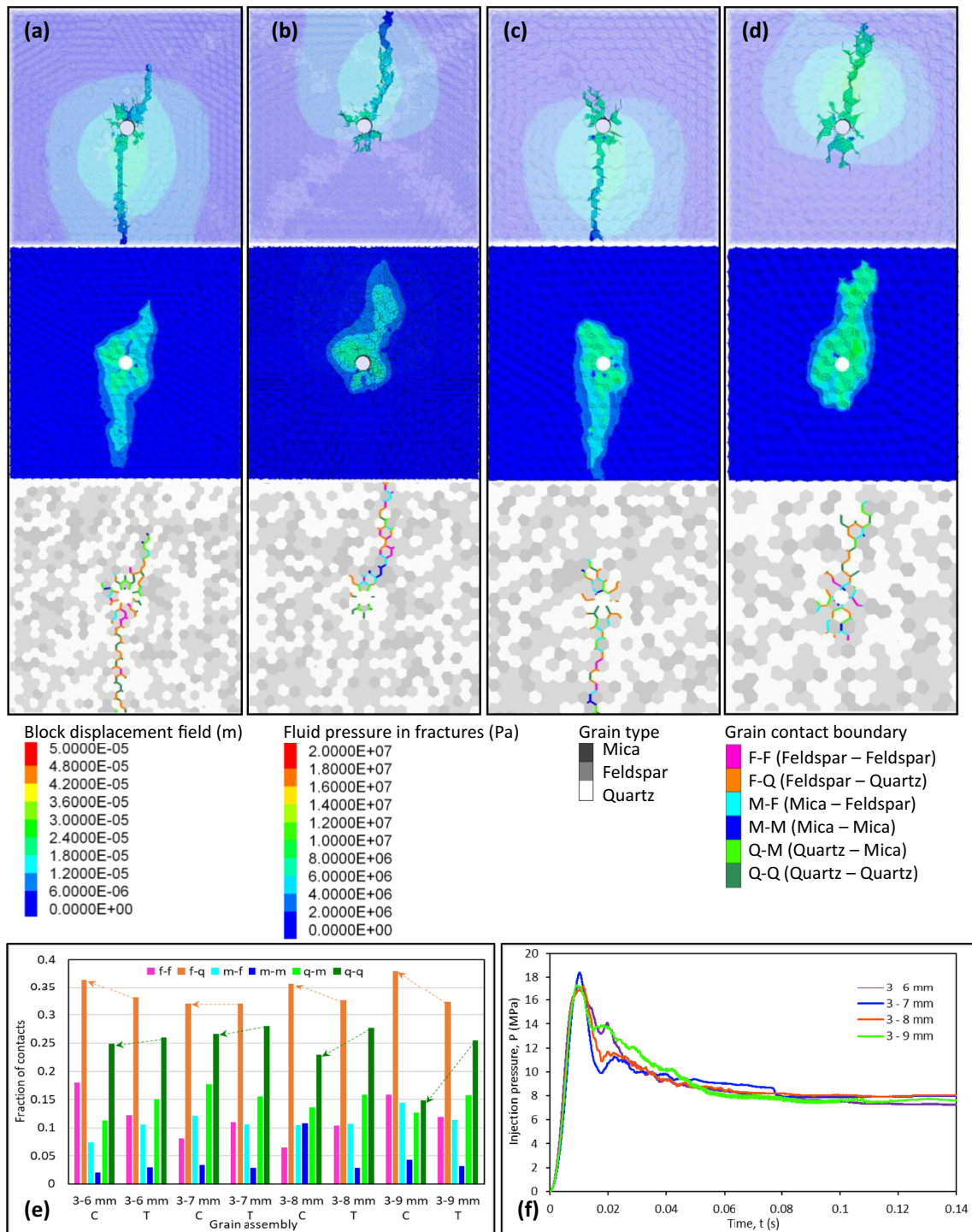
Fig. 14 The effect of grain arrangement and heterogeneity on the HS process. Fluid pressure in fracture and displacement field (background color field), the pressure distribution of matrix fluid leak-off and fracture propagation through different grain boundary types for **a** 3–6 mm, **b** 3–7 mm, **c** 3–8 mm, **d** 3–9 mm particle size distributions, **e** fraction of different contact types in the for the cracked contacts, C and total contacts, T in each grain assembly. The arrows indicate the increase in the fraction of low energy F–Q contacts and the decrease in higher energy Q–Q contacts in the failed contacts, and **f** the fluid injection pressures

on grain boundaries (IG cracks). The second type is cracking, which forms both at grain boundaries and through individual grains (TG cracks) due to induced mechanical stresses. However, as previously discussed, only pre-existing IG cracks were modelled in this study due to computational limitations. Hydraulic simulations were performed on two defect densities for comparison. The defects were modelled by random selection of grain contact boundaries and setting the tensile strength and cohesion of the contact to zero. The two models produced had a percentage of unbonded contacts (fissures) at 5% and 15%. HS was simulated under stress Case 3 ($\sigma_x = 5$ MPa, $\sigma_y = 5$ MPa).

Figure 15a and b show the even distribution of the defects in the models. Forming defects around the injection well were deliberately left out as it would substantially alter the fracture initiation and would not form a basis for direct comparison. Therefore, the fluid pressure build-up of the injection well and the breakdown pressure that corresponds to the fracture initiation were similar for the two models considered. However, the fracture propagation and the fluid leak-off following the breakdown point showed dependence on the pre-defined fissures in the model. Increased fissure density (Fig. 15c and d) contributes to fracture extension. At the same time, a greater distribution of fluid pressure was observed due to fluid leak-off in the fissures. Comparing the strain energy dissipation of the two instances two important aspects are revealed. First, the tensile strain energy dissipation in the contacts is relatively unaffected despite the substantial difference in the defect density. Second, the introduction of fissures tends to have a significant impact on the shearing-induced fractures as the shear strain energy and the subsequent joint friction energy (frictional slip after the shear failure of contacts) in failed contacts increased by 18% and 148%, respectively when the fissure density was increased from 5 to 15%.

5.6 The Effect of Injection Flow Rate on HS

Three injection rates, 18 ml/min, 42 ml/min and 66 ml/min were considered for the simulations to assess the effect of injection flow rate on HS fracture propagation at the grain scale. The fluid viscosity was kept constant and the in-situ stress Case 2 ($\sigma_x = 2.5$ MPa, $\sigma_y = 5.0$ MPa) was used for the simulations. The observed results are shown in Fig. 16. The injection flow rate corresponds to the rate of energy transfer to the system. The increase in fluid injection rate translates to increases in the pressure development in the injection well, the breakdown pressure and the number of fractures around the injection well. Although there is experimental evidence (Zhuang et al. 2022), the reasons for this phenomenon have

not conclusively been proven. However, the increased breakdown pressure can be explained as follows.

As the rate of net energy input to the system (viscosity × injection rate) increases under higher injection rates, a greater amount of strain energy is absorbed by the rock. At lower injection rates, fluid pressure acting on weaker grain boundaries leads to fracturing through grain boundaries and the eventual dissipation of the pore pressure around the injection well. However, at sufficiently high injection flow rates, the fluid pressure is not dissipated and initiates additional cracking around the injection well. Similar observations have been made in other studies where an increased rate of energy input contributes to higher failure stresses and increasingly abrupt drops in the injection pressure (Duan et al. 2018; Fallahzadeh et al. 2017; Kim and Changani 2016; Komurlu 2018; Zhuang et al. 2019).

6 The Hybrid SCDA-HS Pre-conditioning Method

Given the limitations associated with each pre-conditioning method, namely limited fracture growth in SCDA charging and single fracture propagation in HS, the hybrid fracturing method was assessed to improve the fractures generated by pre-conditioning. As explained in Sect. 1.4, the injection well was first charged by SCDA to initiate fractures. Next, the injection well was pressurized by applying a fluid pressure boundary condition to the injection well (see Fig. 9 in Sect. 4.3) where a fluid injection rate of 90 ml/min was maintained. The hybrid fracturing method was simulated under two conditions. First, under anisotropic stress conditions (Case 2: $\sigma_x = 2.5$ MPa, $\sigma_y = 5.0$ MPa) with no defects and second, under stress Case 2 in the presence of 15% fissures in the model, which represent pre-existing defects at the grain scale.

Figure 17a shows the initial fracture pattern produced by SCDA charging for Case 2 and the expansive pressure development is shown in Fig. 17d. It should be noted that the time taken for the SCDA expansion is not representative of the field or experimental conditions (which would be in the order of hours). But rather, the total strain energy released by SCDA was modelled over a shorter period for ease of simulation. As previously shown, SCDA charging produces multiple radial fractures despite the stress anisotropy around the injection well. The fracture extension produced by subsequent fluid injection is shown in Fig. 17b, where fracture extension was observed in five fractures. In comparison, the hydraulic loading of the injection well without prior SCDA
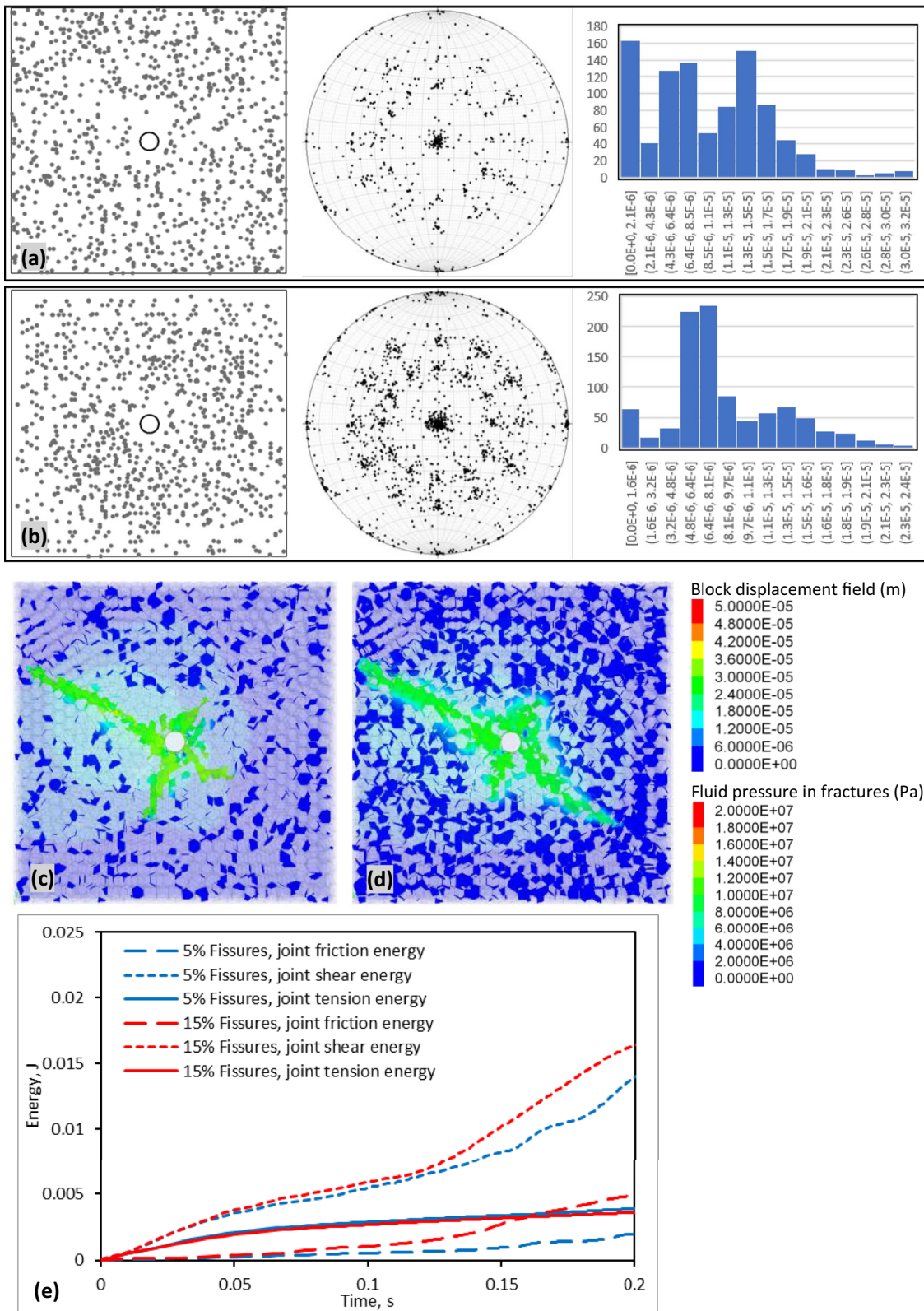
Fig. 15 HS fracture propagation in a fissured granular assembly. Spatial distribution, pole positions in a stereonet, distribution of the defect contact areas (in m^2) for models with (**a** 5% and **b** 15% of contacts defined as defects. HS fracture pattern, block displacement field (background color field) and the fluid pressure leak-off for **c** 5% fissures and **d** 15% fissures, and **e** energy release in contacts during the HS process for the two cases considered
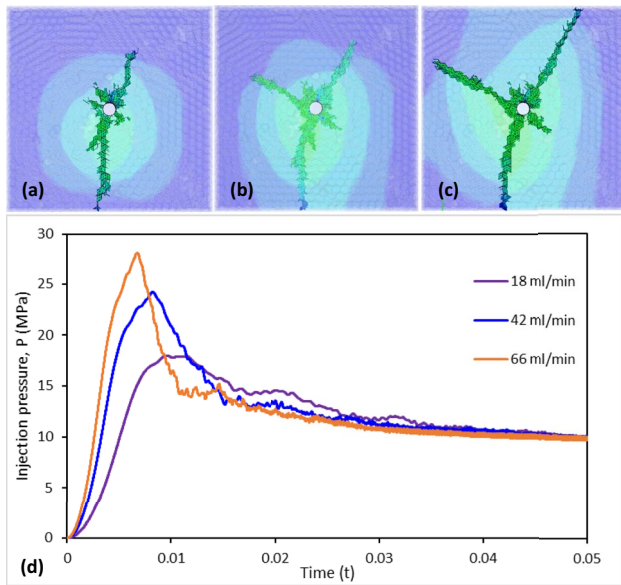
Fig. 16 The influence of energy transmission rate (flow rate) on the HS process. The HS fracture patterns observed for different injection flow rates **a** 18 ml/min, **b** 42 ml/min, **c** 66 ml/min, and **d** the corresponding injection pressure plots

charging only produced 3 cracks (Fig. 17c) but also registered a much higher breakdown pressure of 31.2 Mpa.

The expansive pressure development in the injection well during hybrid SCDA charging, and a comparison of fluid pressures in the injection well for the HS and hybrid fracturing are also shown in Fig. 17d. Since the fractures around the injection well are already initiated before fluid injection in the hybrid method, the sudden drop in the injection pressure observed in pure HS pre-conditioning is not observed during the hybrid fracturing process. Instead, multiple peaks corresponding to fracture extension and a gradual reduction in the injection pressure were observed. This reduction in the breakdown pressure and the absence of an abrupt drop in injection pressure could further contribute to the mitigation of uncontrolled fracture propagation and possibly induced seismicity that is often seen in pure HS.

The performance of the proposed hybrid fracturing method in the presence of 15% micro-fractures is illustrated in Fig. 18. Figure 18a shows the SCDA-charged fracture pattern observed for the first stage of hybrid fracturing. A comparison of the expansive pressures and the injection

pressures developed during hybrid fracturing for 0% and 15% pre-existing fissures is shown in Fig. 18d. The expansive pressure development during SCDA charging was nearly identical for 0% and 15% fissures (Fig. 18d). Yet, the SCDA-charged fracture exhibited an elongation in the major principal stress direction, which may have been caused by the coalescence of fissures in the rock matrix (See Figs. 17a and 18a). However, for the fluid injection stage of hybrid fracturing, inferior fracture propagation results were observed in the presence of fissures (Fig. 18b) compared to the case of no fissures (Fig. 17b). This lack of fracture extension during the fluid injection can be attributed to increased fluid leak-off into the matrix with the introduction of fissures. This dispersed fluid pressure distribution observed within the rock matrix during the fluid injection is shown in Fig. 18c. Furthermore, the comparison shown in Fig. 18d (for 0% and 15% fissures) indicates a lag in the injection pressure build-up and a reduction in the peak injection pressure for the specimen with 15% fissures which is indicative of the increased fluid leak-off into the matrix.

Simulating the hybrid SCDA-HS pre-conditioning method in a numerical rock block with equal dimensions, although computationally intensive on commercially available computer hardware, provides insight into the 3-dimensional morphology of the induced fractures along the axis of the injection well. Material heterogeneity at the grain scale appears to further contribute to the tortuosity of the fractures produced. Figure 19a and b illustrate the fracture patterns observed from the first (SCDA) and second (HS) stages of pre-conditioning of a numerical specimen with $100 \times 100 \times 100$ mm^3 dimensions fractured under stress Case 3 ($\sigma_x = \sigma_y = 5.0$ MPa). Cross sections of the observed fracture profile at planes (1)–(4) in Fig. 19b are shown in Fig. 19c. Comparing the cross sections with the fracture patterns of the rock 'slab' simulations (Fig. 17b), Fig. 19c exhibits a more complex fracture pattern with multiple crack bifurcations in addition to the main radial cracks. The results of the HS stage of the simulation are consistent with laboratory HS experimental observations, where crack bifurcation was also observed near mica grain boundaries (Fig. 19d). This is due to the 3-dimensional effect of crack propagation in the direction of least resistance considering the strength variability between grain contacts as shown by the crack bifurcations at weak grain contacts in the numerical model. This added
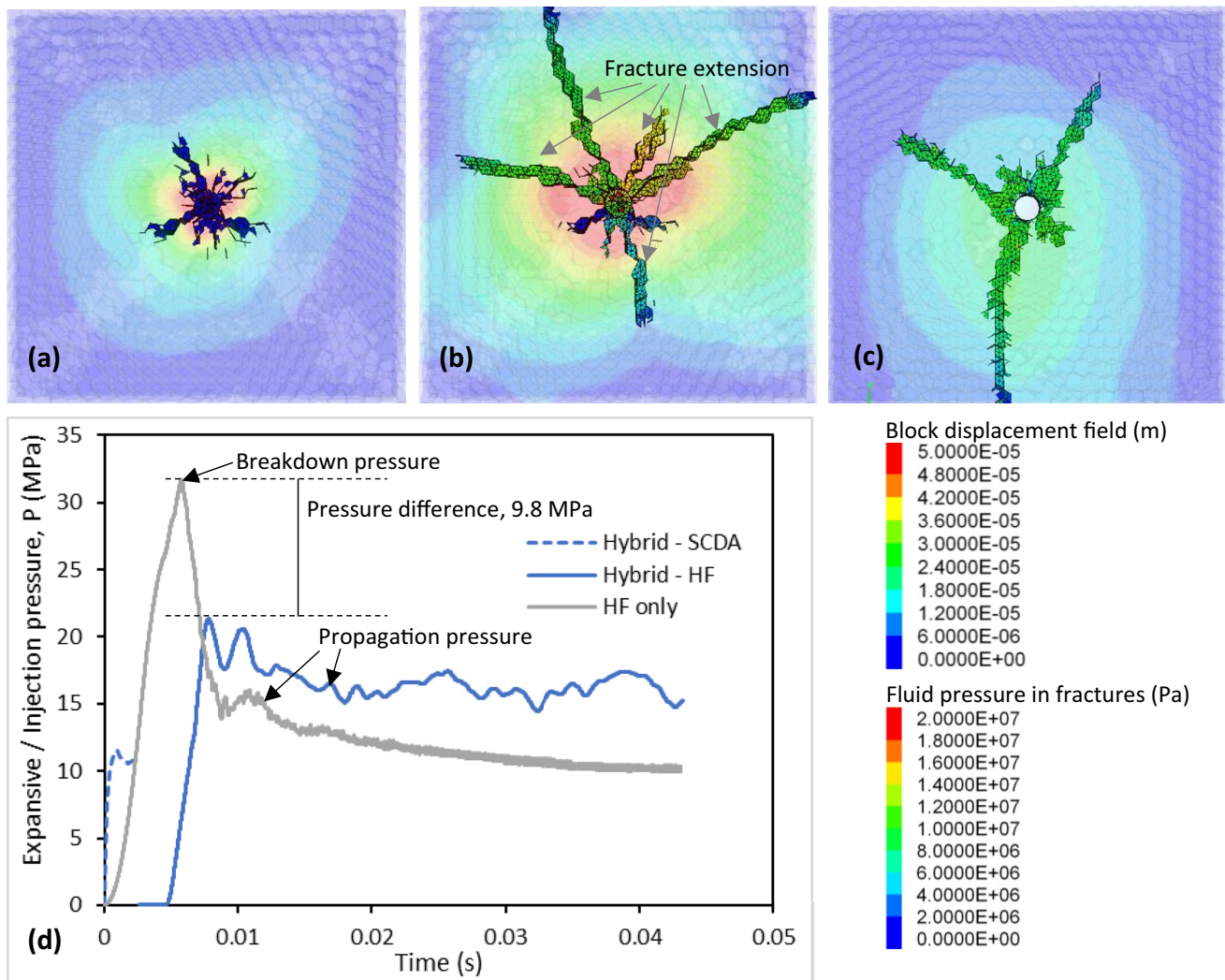
Fig. 17 SCDA-HS hybrid fracture under anisotropic stress conditions (Case 2). **a** Fracture pattern produced by SCDA charging, **b** fracture extension of SCDA-charged specimen by hydraulic loading, **c** fracture pattern produced by HS without SCDA charging, (the back-ground color field indicates block displacement) and **d** Expansive pressure development and fluid injection pressure within injection well for SCDA-HS hybrid fracture and HS only fracture

complexity of the fracture geometry would be beneficial for pre-conditioning applications in low-grade mineral recovery.

7 Conclusions

In this study, we propose a two-stage hybrid rock pre-conditioning method using soundless cracking demolition agents (SCDA) and hydraulic stimulation (HS). W first compared SCDA charging and HS in isolation to evaluate the limitations of each pre-conditioning method. We found that SCDA charging creates multiple radial fractures around an injection well with limited fracture extent, while HS typically produces a single unidirectional fracture. In the proposed hybrid method, SCDA charging is used to initiate multiple radial fractures, followed by HS to extend the fractures.
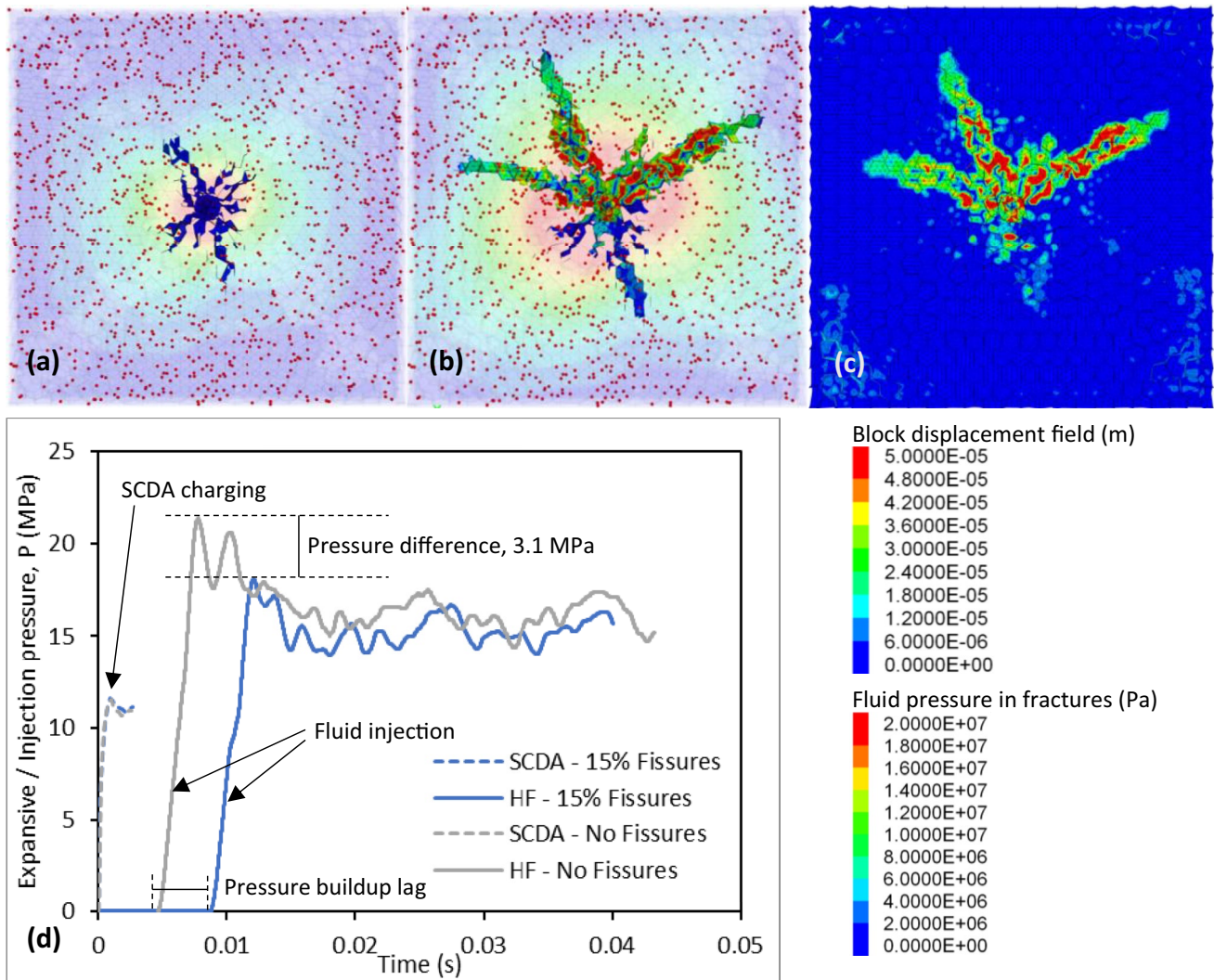
Fig. 18 SCDA-HS hybrid fracture in the presence of pre-existing fissures and anisotropic stress conditions (Case 2). **a** Fracture pattern produced by SCDA charging, **b** fracture extension of SCDA-charged specimen by hydraulic loading, (the red points indicate the position of fissures, and the background color field indicates block displacement) **c** pressure plot of fluid leak-off into the rock matrix, and **d** expansive pressure development and fluid injection pressure within injection well for SCDA-HS hybrid fractures simulated, a comparison with and without fissures

To simulate the SCDA-HS hybrid method on crystalline rock at the grain scale, we employed a fully-coupled hydro-mechanical discrete element model. Our results indicate that the hybrid SCDA-HS method generates additional radial fractures and results in a significant decrease in the breakdown pressure (~30%) which could also help mitigate issues such as uncontrolled fracture propagation and induced seismicity. We also examined other key factors that affect the performance of the hybrid method such as rock mass heterogeneity, in-situ stress anisotropy, and pre-existing defects. The findings from these simulations provide a basis for further experimentation to evaluate the viability of the proposed hybrid pre-conditioning method for applications such as rock mass pre-conditioning for low-grade ore mining.
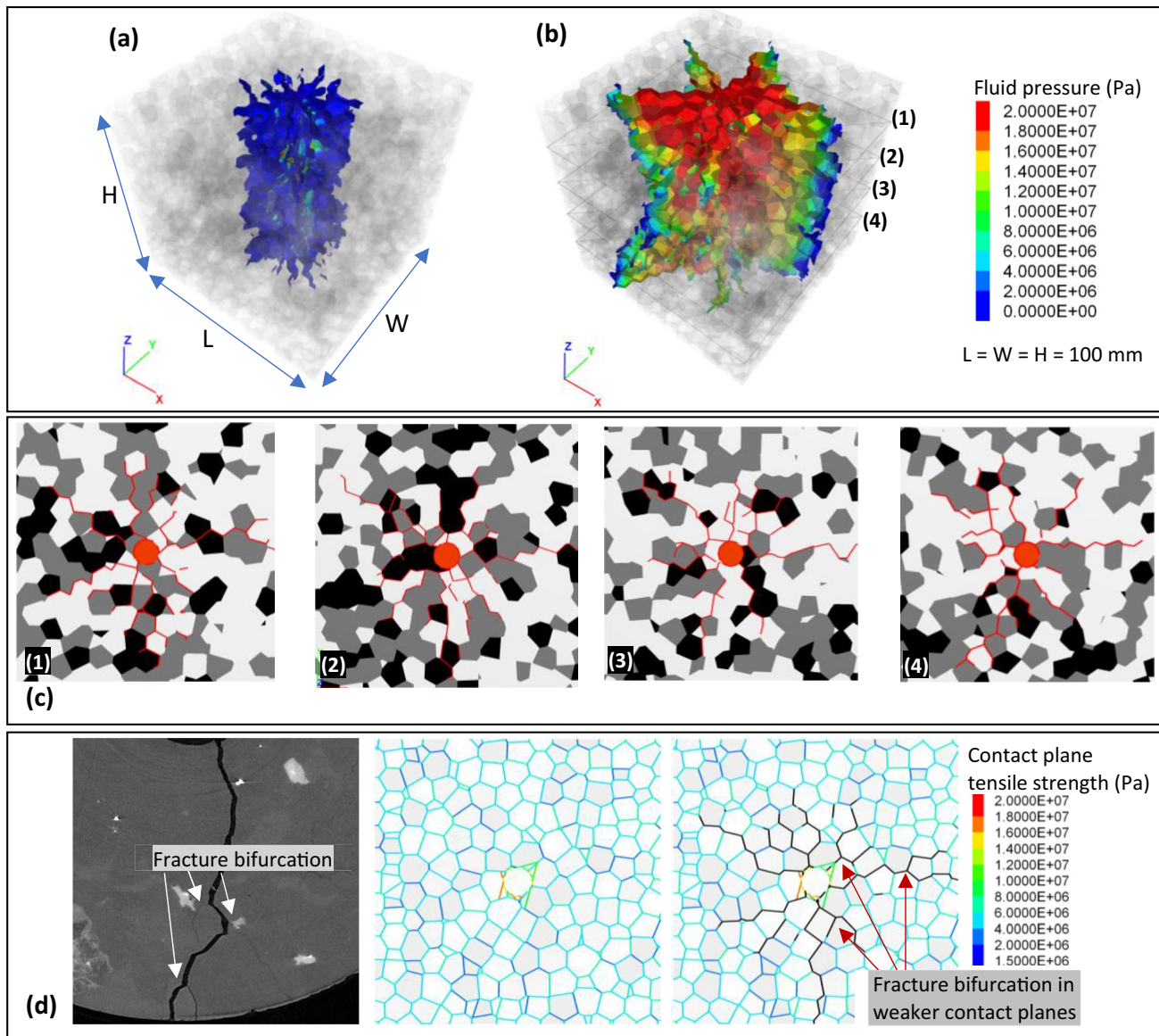
Fig. 19 Effect of grain heterogeneity on the 3-dimensional fracture propagation during hybrid SCDA-HS fracturing under stress Case 3, **a** SCDA-charged fracture, **b** HS fracture extension, **c** cross sections of the model showing complex fractures, and **d** experimentally observed crack branching during HS and crack branching in the numerical model across weak grain boundaries

Data Availability Data sets generated during the current study are available from the corresponding author upon request.

Declarations

Conflict of interest The authors have no competing interests to declare that are relevant to the content of this article.

References

Adams J, Rowe C (2013) Differentiating applications of hydraulic fracturing. In: ISRM international conference for effective and sustainable hydraulic fracturing all days

Ahlness JK, Pojar MG (1983) In situ copper leaching in the United States: case histories of operations. In: US Department of the Interior, Bureau of Mines.

Amorer G, Duffield S, Ross J de, Viegas G (2022) Surface hydraulic fracturing trial at Cadia East, ACG Caving, 30 Aug - 01 Sep, ed. Y Potvin, Australian Centre for Geomechanics, Adelaide

Bear J (1988) Dynamics of fluids in porous media. Courier Corporation, Chelmsford

Bunger AP, Lecampion B (2017) Four critical issues for successful hydraulic fracturing applications. Rock Mech Eng 2017:551–593

Bunger AP, Zhang X, Jeffrey RG (2012) Parameters affecting the interaction among closely spaced hydraulic fractures. SPE J 17(01):292–306

Chacon E, Barrera V, Jeffrey R, van As A (2004) Hydraulic fracturing used to precondition ore and reduce fragment size for block caving, Massmin 2004, 22-25 Aug, ed. Karzulovic A, Alfaro MA, Instituto de Ingenieros de Chile, Chile

Chen Y, Nagaya Y, Ishida T (2015) Observations of fractures induced by hydraulic fracturing in anisotropic granite. Rock Mech Rock Eng 48(4):1455–1461

Chen W, Konietzky H, Liu C, Tan X (2018) Hydraulic fracturing simulation for heterogeneous granite by discrete element method. Comput Geotech 95:1–15

De Silva V, Ranjith PG, Perera M, Wu B, Rathnaweera TD (2017) Investigation of the mechanical, microstructural and mineralogical morphology of soundless cracking demolition agents during the hydration process. Mater Charact 130:9–24

De Silva VR, Ranjith PG, Perera MS, Wu B, Rathnaweera TD (2018a) A modified, hydrophobic soundless cracking demolition agent for non-explosive demolition and fracturing applications. Process Saf Environ Prot 119:1–13

De Silva VR, Ranjith PG, Perera MS, Wu B, Wanniarachchi WA (2018b) A low energy rock fragmentation technique for in-situ leaching. J Clean Prod 204:586–606

De Silva V, Konietzky H, Märten H, Ranjith PG, Lei Z, Xu T (2023) Numerical simulation of crystalline rock fracturing using soundless cracking demolition agents for in-situ preconditioning. Comput Geotech 155:105187

Dontsov EV (2016) An approximate solution for a penny-shaped hydraulic fracture that accounts for fracture toughness, fluid viscosity and leak-off. R Soc Open Sci 3(12):160737

Duan K, Kwok CY, Wu W, Jing L (2018) DEM modeling of hydraulic fracturing in permeable rock: influence of viscosity, injection rate and in situ states. Acta Geotech 13(5):1187–1202

Fallahzadeh SH, Hossain MM, James Cornwell A, Rasouli V (2017) Near wellbore hydraulic fracture propagation from perforations in tight rocks: the roles of fracturing fluid viscosity and injection rate. Energies 10(3):359

Farahmand K, Vazaios I, Diederichs MS, Vlachopoulos N (2018) Investigating the scale-dependency of the geometrical and mechanical properties of a moderately jointed rock using a synthetic rock mass (SRM) approach. Comput Geotech 95:162–179

Guo T, Zhang S, Ge H, Qu Z (2015) A novel "Soundless Cracking Agent Fracturing" for Shale gas reservoir stimulation. Int J Environ Sci Dev 6(9):681

Hamidi F, Mortazavi A (2014) A new three dimensional approach to numerically model hydraulic fracturing process. J Pet Sci Eng 124:451–467

Haque N (2022) Life cycle assessment of iron ore mining and processing in iron ore. Elsevier, Amsterdam, pp 691–710

He Q, Suorineni FT, Oh J (2016) Review of hydraulic fracturing for preconditioning in cave mining. Rock Mech Rock Eng 49(12):4893–4910

He Q, Suorineni FT, Oh J (2017) Strategies for creating prescribed hydraulic fractures in cave mining. Rock Mech Rock Eng 50(4):967–993

Huang B, Cheng Q, Zhao X, Kang C (2018) Hydraulic fracturing of hard top coal and roof for controlling gas during the initial mining stages in longwall top coal caving: a case study. J Geophys Eng 15(6):2492–2506

Huff RV, Axen SG, Baughman (eds) (1988) Case history: Van Dyke ISL copper project. In: Society of mining engineers of the American Institute of mining

Itasca CG (2022) Guide to 3DEC documentation. Itasca Consulting Group, Minneapolis. Available from: https://docs.itascacg.com/3dec700/3dec/docproject/source/modeling/introduction/guideto3decdocs.html accessed 10-Jan-2023.

Jeffrey RG, Bunger AP, Lecampion B, Zhang X, Chen ZR, van As A, Allison DP, Beer W de, Dudley JW, Siebrits E, Thiercelin M, Mainguy M (2009) Measuring hydraulic fracture growth in naturally fractured rock. In: SPE annual technical conference and exhibition all days

Kaiser PK, Valley B, Dusseault MB, Duff D (2013) Hydraulic fracturing mine back trials—design rationale and project status. In: ISRM international conference for effective and sustainable hydraulic fracturing all days

Kim E, Changani H (2016) Effect of water saturation and loading rate on the mechanical properties of Red and Buff Sandstones. Int J Rock Mech Min 88:23–28

Komurlu E (2018) Loading rate conditions and specimen size effect on strength and deformability of rock materials under uniaxial compression. Int J Geo-Eng 9(1):17

Kumari W, Ranjith PG, Perera M, Chen BK, Abdulagatov IM (2017) Temperature-dependent mechanical behaviour of Australian Strathbogie granite with different cooling treatments. Eng Geol 229:31–44

Kumari W, Ranjith PG, Perera M, Chen BK (2018) Experimental investigation of quenching effect on mechanical, microstructural and flow characteristics of reservoir rocks: thermal stimulation method for geothermal energy extraction. J Pet Sci Eng 162:419–433

Kumari WGP, Beaumont DM, Ranjith PG, Perera MSA, Avanthi Isaka BL, Khandelwal M (2019) An experimental study on tensile characteristics of granite rocks exposed to different high-temperature treatments. Geomech Geophys Geo-Energy Geo-Resour 5(1):47–64

Kuruppu MD, Obara Y, Ayatollahi MR, Chong KP, Funatsu T (2014) ISRM-Suggested method for determining the mode I static fracture toughness using semi-circular bend specimen. Rock Mech Rock Eng 47(1):267–274

Lei Z, Ranjith PG, Wu B, Silva VRS de (2021) Investigation of the fracture performance of soundless cracking demolition agents (SCDA) in different reservoir rocks. In: 55th U.S. Rock Mechanics/Geomechanics Symposium, ARMA-2021-1749

Lekontsev YM, Sazhin PV (2008) Application of the directional hydraulic fracturing at Berezovskaya Mine. J Min Sci 44:3

Li W, Liu YM, Chen XW, Xia CN, Yao X, Chu JW (2020) Field test and numerical simulation of preconditioning by hydraulic fracturing in hard rock iron mine. In: MassMin 2020: eighth international

conference & exhibition on mass mining, Santiago. University of Chile, Santiago, 264–274

Morales RF, Henriquez JO, Molina RE, Araneda OA, Rojas EG (2007) Rock preconditioning application in virgin caving condition in a panel caving mine, Codelco Chile El Teniente Division. In: Deep Mining 2007: Proceedings of the fourth international seminar on deep and high stress mining. Australian Centre for Geomechanics, 111–120

Morrison DM (2022) Value-production systems for block caving mines, ACG Caving, 30 Aug - 01 Sep, ed. Y Potvin, Australian Centre for Geomechanics, Adelaide

Natanzi AS, Laefer DF, Connolly L (2016) Cold and moderate ambient temperatures effects on expansive pressure development in soundless chemical demolition agents. Constr Build Mater 110:117–127

Pallauta J (1985) Lixiviacion in Situ, Yacimiento Chuqui Sur, Codelco Chile, Division Chuquicamata. In: Instituto de Ingenieros de Minas de Chile 36A Convencion

Savitski AA, Detournay E (2002) Propagation of a penny-shaped fluid-driven fracture in an impermeable rock: asymptotic solutions. Int J Solids Struct 39(26):6311–6337

Seredkin M, Zabolotsky A, Jeffress G (2016) In situ recovery, an alternative to conventional methods of mining: exploration, resource estimation, environmental issues, project evaluation and economics. Ore Geol Rev 79:500–514

Sesetty V, Ghassemi A (2018) Effect of rock anisotropy on wellbore stresses and hydraulic fracture propagation. Int J Rock Mech Min 112:369–384

Shanti NO, Chan VWL, Stock SR, de Carlo F, Thornton K, Faber KT (2014) X-ray micro-computed tomography and tortuosity calculations of percolating pore networks. Acta Mater 71:126–135

Taleghani AD (2010) Fracture re-initiation as a possible branching mechanism during hydraulic fracturing. In: U.S. rock mechanics/geomechanics symposium all days

Tan X, Konietzky H (2019) Numerical simulation of permeability evolution during progressive failure of Aue granite at the grain scale level. Comput Geotech 112:185–196

Tang W, Zhai C, Xu J, Yu X, Sun Y, Cong Y, Zheng Y, Zhu X (2022) Numerical simulation of expansion process of soundless cracking demolition agents by coupling finite difference and discrete element methods. Comput Geotech 146:104699

Wang F, Konietzky H, Herbst M, Chen W (2022a) Mechanical responses of grain-based models considering different crystallographic spatial distributions to simulate heterogeneous rocks under loading. Int J Rock Mech Min 151:105036

Wang H, Xu C, Dowd PA, Wang Z, Faulkner L (2022b) Modelling in-situ recovery (ISR) of copper at the Kapunda mine. Australia Miner Eng 186:107752

Xu S, Hou P, Li R, Cai M (2021) An experimental study on the mechanical properties and expansion characteristics of a novel self-swelling cartridge for rock breakage. Rock Mech Rock Eng 54(2):819–832

Yin T, Wu Y, Li Q, Wang C, Wu B (2020) Determination of double-K fracture toughness parameters of thermally treated granite using notched semi-circular bending specimen. Eng Fract Mech 226:106865

Zeeb C, Konietzky H (2015) Simulating the hydraulic stimulation of multiple fractures in an anisotropic stress field applying the discrete element method. Energy Procedia 76:264–272

Zeng Q-D, Yao J, Shao J (2018) Numerical study of hydraulic fracture propagation accounting for rock anisotropy. J Pet Sci Eng 160:422–432

Zhai C, Xu J, Liu S, Qin L (2018) Fracturing mechanism of coal-like rock specimens under the effect of non-explosive expansion. Int J Rock Mech Min 103:145–154

Zhang F, Dontsov E (2018) Modeling hydraulic fracture propagation and proppant transport in a two-layer formation with stress drop. Eng Fract Mech 199:705–720

Zhou X-P, Li G-Q, Ma H-C (2020) Real-time experiment investigations on the coupled thermomechanical and cracking behaviors in granite containing three pre-existing fissures. Eng Fract Mech 224:106797

Zhuang L, Kim KY, Jung SG, Diaz M, Min K-B (2019) Effect of water infiltration, injection rate and anisotropy on hydraulic fracturing behavior of granite. Rock Mech Rock Eng 52(2):575–589

Zhuang D, Yin T, Li Q, Wu Y, Tan X (2022) Effect of injection flow rate on fracture toughness during hydraulic fracturing of hot dry rock (HDR). Eng Fract Mech 260:108207

Zolfaghari N, Bunger AP (2019) Numerical model for a penny-shaped hydraulic fracture driven by laminar/turbulent fluid in an impermeable rock. Int J Solids Struct 158:128–140

Publisher's Note Springer Nature remains neutral with regard to jurisdictional claims in published maps and institutional affiliations.